(Accepted for Publication in J. Prop. Power 04/April/2018)

LES of Reacting Flows in an Industrial Gas Turbine Combustor

I. Langella[a], Z. X. Chen[b], and N. Swaminathan[c]
Department of Engineering, University of Cambridge, CB2 1PZ Cambridge, UK

S. K. Sadasivuni[d]
Siemens Industrial Turbomachinery Ltd, LN5 7FD Lincoln, UK

The turbulent reacting flow in an industrial gas turbine combustor operating at 3 bar is computed using LES paradigm. The subgrid scale (SGS) combustion is modelled using a collection of unstrained premixed flamelets including mixture stratification. The non-premixed combustion mode is also included using a simple closure involving the scalar dissipation rate of the mixture fraction. A close attention is paid to maintain physical consistencies among sub-closure models for combustion and these consistencies are discussed on a physical basis. The importance of non-premixed mode and SGS mixture fraction fluctuations are investigated systematically. The results show that the SGS mixture fraction variance plays an important role and comparisons to measurements improve when contributions from the premixed and non-premixed modes are included. These numerical results and observations are discussed on a physical basis along with potential avenues for further improvements.

[a] Research Associate, il246@cam.ac.uk
[b] Research Associate, zc252@cam.ac.uk
[c] Professor, ns341@cam.ac.uk
[d] Engineer, suresh.sadasivuni@siemens.com

Nomenclature

Acronyms

CFL - Courant-Friedrichs-Lewy number

CRZ - central recirculation region

CVC - central vortex core

LES - large eddy simulation

ORZ - outer recirculation region

PDF - probability density function

RANS - Reynolds averaged Navier-Stokes

SDR - scalar dissipation rate

SGS - sub-grid scale

TKE - turbulent kinetic energy

Roman

c - scaled progress variable

C_p - specific heat capacity at constant pressure ($\mathrm{kJ\,Kg^{-1}\,K^{-1}}$)

$\mathcal{D}$ - molecular diffusivity ($\mathrm{m^2\,s^{-1}}$)

D - pre-chamber diameter (m)

h - enthalpy (sensible + formation) per unit mass ($\mathrm{kJ\,Kg^{-1}}$)

Δh_f^0 - enthalpy of formation ($\mathrm{kJ\,Kg^{-1}}$)

$\mathcal{K}$ - resolved turbulent kinetic energy ($\mathrm{m^2\,s^{-2}}$)

k - SGS kinetic energy ($\mathrm{m^2\,s^{-2}}$)

p - pressure ($\mathrm{N\,m^{-2}}$)

P - probability density function

$\mathcal{Q}$ - $k/\left(k+\mathcal{K}\right)$

r - radial coordinate (m)

s_L - unstrained planar laminar flame speed ($\mathrm{m\,s^{-1}}$)

t - time (s)

T - temperature (K)

u' - rms velocity scale for turbulent fluctuations ($\mathrm{m\,s^{-1}}$)

U_i - velocity component in direction i ($\mathrm{m\,s^{-1}}$)

x - axial coordinate (m)

Y_k - mass fraction of species k

Da - Damköhler number

Ka - Karlovitz number $= \tau_c/\tau_\eta$

Sc - Schmidt number

Greek

β_c - combustion model parameter

χ_ϕ - scalar dissipation rate of scalar ϕ

δ - Zeldovich flame thickness (m)

δ_{th} - laminar flame thermal thickness (m)

Δ - filter width

ϵ_k - TKE dissipation rate ($\mathrm{m^3\,s^{-3}}$)

$\widetilde{\varepsilon}_j$ - sub-grid scale scalar dissipation rate of scalar j ($\mathrm{s^{-1}}$)

η - sample variable space for ξ

Λ - turbulent integral length scale (m)

μ - dynamic viscosity ($\mathrm{Kg\,m^{-1}\,s^{-1}}$)

$\dot{\omega}$ - reaction rate ($\mathrm{Kg\,m^{-3}\,s^{-1}}$)

ψ - unscaled progress variable

ρ - density ($\mathrm{Kg\,m^{-3}}$)

σ_j^2 - variance of scalar j

τ - heat release parameter

τ_c - chemical time scale

τ_η - Kolmogorov time scale

ξ - mixture fraction

ζ - sample space variable for c

Superscripts

$*$ - normalised variable

eq - equilibrium value

Subscripts

ad - adiabatic condition

b - burnt condition

ct - mixed mode contribution

fp - premixed mode contribution

np - non-premixed mode contribution

rms - root mean square

sgs - sub-grid scale

st - stoichiometry

u - unburnt condition

Operators

$\overline{\Phi}$ - Reynolds filtered value of Φ

$\widetilde{\Phi}$ - Favre filtered value of Φ

$\langle\Phi\rangle$ - time-averaged value of Φ

D/Dt - substantial derivative

I. Introduction

Fuel lean combustion is of interest for power generation as it can deliver both high efficiency and low emissions [1], but the ignition and combustion stability of lean mixtures present challenges for its practical use. The potential risks including flashback and structural damage due to thermoacoustics are overcome by careful design of combustor aerodynamics and using active or passive control strategies for fuel injection. Consequently, lean combustors involve complex swirling flow with varying levels of fuel-air mixing. Hence, turbulent partially premixed combustion occurs in these

combustors. Thus, the ability of reacting flow CFD (Computational Fluid Dynamics) to capture these phenomena is crucial for their use in the design of next-generation combustors [2].

Past studies have demonstrated that Large Eddy Simulation (LES) is suitable to capture aerodynamics of swirling flows, and the continuous increase of computing power allows application of LES-based models to practical burners [3–7]. Combustion requires modelling as it is a subgrid phenomenon in LES. Closures developed for the subgrid scale (SGS) reaction rate include: dynamic thickened flame model [8, 9], linear eddy model [10], fractal flame-wrinkling model [11], partially-stirred reactor model [12], and Eulerian stochastic fields [13]. Another recently developed flamelet model for LES uses Scalar Dissipation Rate (SDR) closure [14, 15], which is shown to be successful in RANS studies of industrial gas turbine combustors [16, 17], but this approach has not been tested for LES of reacting flows in these combustors. This provides the motivation for this work.

Due to large costs for experiments at realistic operating conditions of gas turbines (i.e. with optical access, high pressure, and preheated air), high quality validation data is rare [18]. One widely studied database is the set of laser-diagnostics obtained for Siemens SGT-100 combustor at 3 bar [19]. Analyses of these measurements and past LES results suggest that the combustion has flamelet-like properties despite the highly turbulent flow [5–7, 20, 21]. Flamelet models assume that the combustion time scale, $\tau_c = s_L/\delta$ is shorter than the smallest turbulent scales (this also applies for length scales) implying that the flamelet structure is undisturbed by the turbulence. Thus, the SGS reaction rate can be calculated *a priori* using laminar flamelets. Hence, this methodology is also known as tabulated chemistry approach.

Turbulent eddies can penetrate the flame-front disturbing its internal structure in high Karlovitz number, $\mathrm{Ka} = \tau_c/\tau_\eta$, combustion which is also known as distributed combustion. Modelling this regime of turbulent combustion using flamelet approach is thus an open question. However, flamelet-like structures were observed in high Ka combustion in past studies, see for example [22–28]. It was pointed out that this regime could be viewed as *distributed flamelets* combustion and the premixed flamelet approach worked quite well as long as the physical consistencies were maintained among various sub-closures used in LES [28]. These consistencies are discussed later.

The objective of this study is two-fold, viz., (i) to test and investigate the performance of the

flamelet approach for combustion conditions of the SGT-100 investigated experimentally in [19] and, (ii) to identify limitations of this approach and its sensitivity to fuel-air mixing variation, signified by mixture fraction variance. Specifically, the second objective helps to systematically understand the contributions of non-premixed mode to partially premixed combustion in the SGT-100. A cross comparison of the current results to those published for the SGT-100 using other SGS closures is discussed in the Appendix. The experimental and LES setup are discussed in Sections II and III respectively. The detail of the flamelet closure used here is discussed in Section III B along with a discussion on the necessary physical consistencies to be maintained in the combustion modelling framework. Results are discussed in Section IV and conclusions are drawn in the final section.

II. Test Case - TurChemi Experiments

The SGT-100 burner featuring a square-sided combustion chamber with optical access for laser diagnostics as shown in Fig. 1a [19] was studied using high pressure test facility at DLR. The combustion chamber was a modified version of the commercial dry low emission combustor of the SGT-100 family of Siemens, with six combustors delivering a nominal shaft power of 5.7 MW. Pre-heated air at 685 K entered the radial swirler having 12 rectangular channels each with multiple small holes to inject natural gas at 305 K which is taken to be 100% CH_4 following earlier studies. The inlet air mass flow rate including panel cooling air was 183.8 g/s and the fuel flow rate was 6.2 g/s for the 3 bar test case reported in [19] as Case A. The uncertainties in the air and fuel mass flow rates were $\pm 4\%$ and $\pm 3\%$ respectively [19] and these flow rates gave an overall equivalence ratio of $\phi \approx 0.6$. The various dimensions for this combustor are shown in Fig. 1a along with 4 measurement planes used in the experiments [19]. The first plane is at 18.7 mm from the prechamber lip (not shown in the figure). The second, third and fourth planes are located respectively at 20, 40 and 70 mm from the first plane. The combustion conditions in these planes were noted [19] to be in the border between the thin reaction zones and distributed reaction zones regimes of the turbulent combustion diagram [29]. The Damköhler number, $\mathrm{Da} = (\Lambda\, s_L/u'\delta)$, was noted to be in the range of $1.4 \leq \mathrm{Da} \leq 2.5$ with $77 \leq \mathrm{Ka} \leq 230$ as shown in Fig. 1b. The rms of turbulent velocity fluctuation is u' and its integral length scale is Λ. Detailed interrogation [6] of the measured OH suggested that there were flamelets embedded in an environment of distributed combustion

although the combustion conditions were in the border between thin and distributed reaction zones regimes [19]. This supports the idea of distributed flamelets regime combustion for high Ka flames proposed in [28]. Hence, it is of interest to assess the performance of flamelet-based modelling for the SGT-100 combustor as it has not been attempted earlier.

There is a large database of in-flame measurements including Particle Image Velocimetry (PIV), OH^* chemiluminescence, OH Planar Laser Induced Fluorescence (PLIF), and 1D-Raman spectroscopy. The latter includes traverses for species concentrations and temperature at the 4 axial locations noted above, which correspond to $x/D = 1.21$, 1.44, 1.66 and 2.00 in the CFD coordinates, where $D = 86\,\text{mm}$ is the pre-chamber diameter noted in Fig. 1a. The experimental error associated with temperature is about 6% for reactant mixture and goes up to 13% for the burnt mixture [5, 19]. Errors of 6%, 5% and 4% were reported for O_2, N_2 and CH_4 mass fractions respectively in the unburnt mixture. The errors for CO_2, O_2, N_2 and H_2O in the products were 20%, 21%, 6% and 14% respectively [5, 19].

III. LES Detail

A. Governing equations

A finite volume based unstructured CFD code [30], OpenFOAM, is used for this study. This code solves filtered conservation equations for mass, momentum, and energy along with other equations required for combustion modelling. The equations for mass and momentum are respectively

$$\frac{\partial \overline{\rho}}{\partial t} + \frac{\partial \overline{\rho}\widetilde{U}_i}{\partial x_i} = 0, \qquad \text{and} \tag{1}$$

$$\overline{\rho}\frac{D\widetilde{U}_i}{Dt} = \frac{\partial}{\partial x_j}\left(\widetilde{\mu}\frac{\partial \widetilde{U}_i}{\partial x_j}\right) - \frac{\partial \overline{p}}{\partial x_i} - \frac{\partial \tau^r_{ij}}{\partial x_j}, \qquad i = 1, 2, 3 \tag{2}$$

where $\widetilde{U}_i$ is the velocity in direction i, $\overline{p}$ is the modified filtered pressure, which is the sum of filtered pressure and $2k/3$ with k as the SGS kinetic energy [31]. The symbol $\mu = \rho\nu$ is the dynamic viscosity of the fluid. The filtered kinematic viscosity is obtained using the Sutherland's law, $\overline{\rho\nu} \approx A_s\sqrt{\widetilde{T}}/\left(1 + T_s/\widetilde{T}\right)$, where $A_s \approx 1.67 \times 10^{-6}$ is a dimensional constant and $T_s \approx 170.7\,\text{K}$.

The subgrid stresses are closed using $\tau^r_{ij} = -2C_k\,\Delta\,\overline{\rho}\,\sqrt{k}\,\left(\widetilde{S}_{ij} - \widetilde{S}_{kk}/3\right)$, where τ^r_{ij} is the anisotropic part of the residual stress tensor $\tau^R_{ij} = \tau^r_{ij} + 2k\,\delta_{ij}/3$, $\widetilde{S}_{ij}$ is the Favre-filtered symmetric strain tensor, $C_k \approx 0.1$ and δ_{ij} is the Kronecker delta [31]. The filter width is Δ, which is

typically taken as the cube root of the numerical cell volume. The SGS kinetic energy k is obtained using [32],

$$\overline{\rho}\frac{Dk}{Dt} \approx \frac{\partial}{\partial x_j}\Big[\Big(\widetilde{\mu}+\widetilde{\mu}_t\Big)\frac{\partial k}{\partial x_j}\Big] + \widetilde{U}_i\frac{\partial \tau_{ij}^R}{\partial x_j} - \overline{\rho}\epsilon_k + \Pi \tag{3}$$

where $\widetilde{\mu}_t = C_k\,\Delta\,\overline{\rho}\,\sqrt{k}$ is the SGS viscosity. The dissipation rate of k is modelled as $\epsilon_k \approx C_\epsilon\,k^{3/2}/\Delta$ with $C_\epsilon \approx 0.7$ [31]. The SGS pressure-work term, Π, is neglected based on previous LES study [33]. The partially premixed combustion modelling used for the SGT-100 combustor is described next.

B. Combustion closure

The partially premixed combustion includes premixed and non-premixed modes. If the reactant mixture at a given point is within the flammability limits then the combustion is expected to be in premixed mode. The non-premixed combustion typically occurs in stoichiometric regions where diffusion processes aided by turbulence bring fuel and oxidiser together. This mixing is described using the mixture fraction, ξ, and the reaction progress in premixed mode is denoted using a reaction progress variable, c. The local thermo-chemical state of the mixture is thus described using these two variables. The mixture fraction is defined using Bilger's formula [34] and its filtered value is transported using

$$\overline{\rho}\frac{D\widetilde{\xi}}{Dt} = \nabla\cdot\Big[\Big(\overline{\rho\mathcal{D}}+\frac{\mu_t}{Sc_t}\Big)\nabla\widetilde{\xi}\Big] \tag{4}$$

where $\widetilde{\mathcal{D}} = \overline{\rho\mathcal{D}}/\overline{\rho} \approx \widetilde{\mu}/0.7$ is the filtered molecular diffusivity which is taken to be the same for all scalars (unity Lewis number) and $Sc_t \approx 0.7$ is the SGS Schmidt number.

The progress variable varying between 0 and 1 is defined as $c = \psi/\psi^{eq}$, where ψ is defined using either temperature or an appropriate combination of species mass fractions and ψ^{eq} is the corresponding equilibrium value, which is approximated to be the flamelet burnt value. Here, $\psi \equiv (Y_{\mathrm{CO2}} + Y_{\mathrm{CO}})$ is used following earlier studies [28, 35]. Out of many possible definitions for c [36], this particular definition guarantees a monotonic variation of c for all values of mixture fraction [37]. The transport equation for $\widetilde{c}$ is

$$\overline{\rho}\frac{D\widetilde{c}}{Dt} = \nabla\cdot\Big[\Big(\overline{\rho\mathcal{D}}+\frac{\mu_t}{Sc_t}\Big)\nabla\widetilde{c}\Big] + \overline{\dot{\omega}}^* \tag{5}$$

The filtered reaction rate $\overline{\dot{\omega}}^*$ is given as [38, 39]

$$\overline{\dot{\omega}^*} = \overline{\dot{\omega}}_c + \overline{\rho\,\chi_{\xi\xi}\frac{c}{\psi^{eq}}\frac{d^2\psi^{eq}}{d\xi^2}} + 2\,\overline{\rho\,\chi_{\xi\,c}\frac{1}{\psi^{eq}}\frac{d\psi^{eq}}{d\xi}} = \overline{\dot{\omega}}_{\rm fp} + \overline{\dot{\omega}}_{\rm np} + \overline{\dot{\omega}}_{\rm ct}, \tag{6}$$

where $\chi_{\xi\,\xi} \equiv \chi_\xi = \mathcal{D}(\nabla\xi\cdot\nabla\xi)$ is the instantaneous scalar dissipation rate of the mixture fraction and $\chi_{\xi\,c}$ is the cross dissipation rate. The first part, $\overline{\dot{\omega}}_{\rm fp}$, of Eq. (6) signifies premixed (with mixture stratification) mode contribution, $\overline{\dot{\omega}}_{\rm np}$ signifies non-premixed mode contribution and $\overline{\dot{\omega}}_{\rm ct}$ denotes mixed mode contribution resulting from interactions of ∇c and $\nabla\xi$. The third contribution was shown to be an order of magnitude smaller than the other two in previous studies [39–42] and, it is neglected here for consistency with the joint PDF closure for Eq. (7) and for the sake of simplicity since including $\overline{\dot{\omega}}_{\rm ct}$ would introduce additional modelling and uncertainties. The effects of cross-correlations will be investigated in future, for example using copula method [41, 43].

The premixed part is estimated using

$$\overline{\dot{\omega}}_{\rm fp} \;=\; \int_0^1\int_0^1 \dot{\omega}(\zeta,\eta)\;P(\zeta,\eta)\quad {\rm d}\zeta\;{\rm d}\eta, \tag{7}$$

where ζ and η are sample space variables for c and ξ respectively and $P(\zeta,\eta)$ is the SGS joint PDF. The flamelet reaction rate $\dot{\omega}(\zeta,\eta)$ is obtained from unstrained planar laminar premixed flames computed over the whole range of ξ spanning the flammability limits. This approach is different from the flamelet/progress-variable (FPV) approach of Pierce and Moin [44] who employed diffusion flamelets parameterised using a progress variable instead of the natural choice χ_ξ. Furthermore, distinguishing premixed and non-premixed combustion contributions as in Eq. (6) is not possible in the FPV approach.

The non-premixed contribution, $\overline{\dot{\omega}}_{\rm np}$, is estimated using [35, 41, 42, 45, 46]

$$\overline{\dot{\omega}}_{\rm np} \;\approx\; \overline{\rho}\,\widetilde{c}\,\widetilde{\chi}_\xi \int_0^1 \frac{1}{\psi^{eq}(\eta)}\,\frac{{\rm d}^2\psi^{eq}(\eta)}{{\rm d}\eta^2}\,P(\eta)\quad {\rm d}\eta, \tag{8}$$

where $\widetilde{\chi}_\xi = \widetilde{\mathcal{D}}\left(\nabla\widetilde{\xi}\cdot\nabla\widetilde{\xi}\right) + \widetilde{\varepsilon}_\xi$ is the Favre filtered scalar dissipation rate of the mixture fraction, which is the sum of resolved and SGS contributions. The latter is computed using a linear relaxation model: $\widetilde{\varepsilon}_\xi = C_\xi(\nu_t/\Delta^2)\sigma^2_{\xi,{\rm sgs}}$, where $\sigma^2_{\xi,{\rm sgs}}$ is the SGS variance of ξ which needs a closure and $\nu_t = \mu_t/\overline{\rho}$ is the SGS viscosity (see Section III A). The model parameter is $C_\xi = 2$ following earlier studies [3]. One can also use diffusion rather than premixed flamelets to evaluate Eq. (8). However,

the difference in $\overline{\dot{\omega}}_{\rm np}$ obtained using these two types of flamelets are observed to be small for the conditions of this study and so premixed flamelets are preferred in order to keep consistencies with Eq. (7). Moreover, $\overline{\dot{\omega}}_{\rm np}$ is small compared to $\overline{\dot{\omega}}_{\rm fp}$ as will be seen later. So, the conclusions of this work does not depend on the choice for the flamelet type used for $\overline{\dot{\omega}}_{\rm np}$.

The joint PDF in Eq. (7) is $P(\zeta,\eta) = P(\zeta)\,P(\eta|\zeta) \simeq P(\zeta)P(\eta)$, which assumes statistical independence between ζ and η. This assumption is quite common in LES of reacting flows while a more general approach would include SGS covariance of c and ξ which would require further closures to be developed in future studies. The marginal PDFs of c and ξ are modelled using Beta functions [47], for example $P(\eta) = \beta(\eta;\,\widetilde{\xi},\sigma^2_{\xi,\rm sgs})$ for ξ, where the subgrid variance $\sigma^2_{\xi,\rm sgs}$ is obtained from its transport equation:

$$\overline{\rho}\frac{D\sigma^2_{\xi,\rm sgs}}{Dt} \;\approx\; \nabla\cdot\Big[\Big(\overline{\rho\mathcal{D}}+\frac{\mu_t}{Sc_t}\Big)\nabla\sigma^2_{\xi,\rm sgs}\Big] - 2\,\overline{\rho}\,\widetilde{\varepsilon}_\xi + 2\,\overline{\rho}\,\frac{\nu_t}{Sc_t}\left(\nabla\tilde{\xi}\cdot\nabla\tilde{\xi}\right), \tag{9}$$

where $\widetilde{\varepsilon}_\xi$ is modelled using the linear relaxation model noted above. The marginal PDF of ξ becomes $P(\eta) = \delta(\eta-\widetilde{\xi})$ for $\sigma^2_{\xi,\rm sgs} = 0$ because the Beta function degenerates to a delta function if the variance is zero. This allows us to systematically investigate the effect of $\sigma^2_{\xi,\rm sgs}$ as discussed in Section III D 1.

The Beta PDF for c requires the SGS variance $\sigma^2_{c,\rm sgs}$, which is obtained using

$$\overline{\rho}\frac{D\sigma^2_{c,\rm sgs}}{Dt} \;\approx\; \nabla\cdot\Big[\Big(\overline{\rho\mathcal{D}}+\frac{\mu_t}{Sc_t}\Big)\nabla\sigma^2_{c,\rm sgs}\Big] - 2\overline{\rho}\,\widetilde{\varepsilon}_c + 2\,\overline{\rho}\,\frac{\nu_t}{Sc_t}\left(\nabla\widetilde{c}\cdot\nabla\widetilde{c}\right) + 2\,\left(\overline{c\,\dot{\omega}}^* - \widetilde{c}\,\overline{\dot{\omega}}^*\right). \tag{10}$$

The reaction related term $\overline{c\,\dot{\omega}}^*$ is modelled in a manner consistent with Eq. (7). The subgrid SDR, $\widetilde{\varepsilon}_c$, is modelled using a well tested algebraic expression [14, 28, 35, 48, 49]:

$$\widetilde{\varepsilon}_c = \left[1-\exp\left(\frac{-0.75\Delta}{\delta_{th}}\right)\right]\left[(2K_c-\tau C_4)\,\frac{s_L}{\delta_{th}} + C_3'\frac{\epsilon_k}{k}\right]\frac{\sigma^2_{c,\rm sgs}}{\beta_c} \tag{11}$$

where k and ϵ_k are the subgrid kinetic energy and its dissipation rate respectively. The thermo-chemical parameter K_c is 0.79τ, where $\tau = (T_{ad}-T_u)/T_u$ is the heat release parameter. The reactant and adiabatic flame temperatures are denoted using T_u and T_{ad} respectively. The mixture fraction dependent flamelet quantities, s_L, δ_{th}, and τ are obtained from flamelet calculations. The subgrid SDR must also be proportional to dissipation time scale for k and this part is given by the term involving $C_3' \approx 1.2\sqrt{\rm Ka_\Delta}/(1+\sqrt{\rm Ka_\Delta})$ in Eq. (11), where ${\rm Ka_\Delta} = \sqrt{\epsilon_k\,\delta_{th}}/s_L^{3/2}$. The other parameter is $C_4 = 1.1/(1+{\rm Ka_\Delta^{0.4}})$. These parameters and constants are derived using DNS data in

past studies and they are not tuneable. The values used here are exactly the same as those used in past studies [28, 35, 48, 49]. The only adjustable parameter β_c is obtained dynamically [28, 48–50].

Other SDR models, which are predominantly empirical and for RANS, proposed in past studies are reviewed in [51]. These models do not include the competing effects of turbulence and chemical reactions in combustion. For example, the model proposed by Borghi and his co-workers [52–55] excluded the heat release effects by assuming constant density and it was addressed by Kuan *et al.* [56] somewhat by including $\rho_u\, s_L/\left(\overline{\rho}\, v_\eta\right)$, where v_η is the Kolmogorov velocity. This modification was empirical based on fractal approach and this ratio was multiplied by the term involving C_3' in Eq. (11) to model the SDR. More importantly, these models do not include the change in the scalar mixing physics observed in turbulent premixed flame [57, 58], which is represented by the term involving negative C_4 in Eq. (11). More elaborate discussion on the comparison of these models may be found in [51].

The flamelet approach described above allows tabulation of the filtered reaction rate as a function of 4 controlling variables, $\widetilde{\xi}$, $\widetilde{c}$, $\sigma^2_{c,\mathrm{sgs}}$ and $\sigma^2_{\xi,\mathrm{sgs}}$, which are transported in the LES. The reaction rate is retrieved from the look-up table during the LES and the construction of this table is described in Section III D. It is worth to note that $\overline{\dot{\omega}}^* \rightarrow \dot{\omega}^*(c,\, \xi)$ for a numerical grid resolving most of the fluctuations to yield $\sigma^2_{\xi,\mathrm{sgs}} = \sigma^2_{c,\mathrm{sgs}} \approx 0$ and thus the right flame propagation speed is recovered in regions with quasi-laminar conditions.

The filtered enthalpy (sum of sensible and formation enthalpies) of the mixture is computed using

$$\overline{\rho}\frac{D\widetilde{h}}{Dt} = \nabla\cdot\Big[\Big(\overline{\rho\mathcal{D}} + \frac{\mu_t}{Sc_t}\Big)\nabla\widetilde{h}\Big]. \tag{12}$$

This allows to include sub-adiabatic streams that may be present in the system. Hence, the local mixture temperature is calculated from $\widetilde{h}$ as $\widetilde{T} = T_0 + \left(\widetilde{h} - \widetilde{\Delta h^0_f}\right)/\widetilde{C}_{p,\mathrm{eff}}$, where $T_0 = 298.5$ K and $\widetilde{\Delta h^0_f}$ is the enthalpy of formation computed as described in [41]. The temperature dependent effective specific heat capacity of the mixture is obtained as $C_{p,\mathrm{eff}} = (T - T_0)^{-1}\int_{T_0}^{T} C_p(T^*)\ \mathrm{d}\,T^*$ where C_p is the constant pressure specific heat capacity of the mixture [41]. The mixture density at temperature $\widetilde{T}$ is computed using the ideal gas state equation. One can also use the temperature, density and fluid properties obtained from flamelets for adiabatic systems. However, using Eq. (12)

keep the approach general and so it is followed here. This modelling approach worked well for various flames in a range of flow and combustion conditions [17, 28, 35, 42, 48, 49] as it maintains physical consistencies, which are remarked next.

1. Note on physical consistencies

Typically there is no variance of c at the inlet boundaries and it is produced predominantly by combustion. Its production by turbulence can occur only if $\nabla\widetilde{c}$ is present. This gradient can result from the mixing of hot products ($\widetilde{c}=1$) with cold mixture but one must recognise that combustion is the dominant mechanism to produce $\nabla\widetilde{c}$ as c changes from 0 to 1 in a narrow region (flame). Thus, one must be cautious while modelling $\widetilde{\varepsilon}_c$ as noted in many earlier studies [54, 55, 59]. The reaction related term in Eq. (10) cannot be ignored while modelling $\widetilde{\varepsilon}_c$ because it is leading order as demonstrated in [49] for LES. Hence, a linear relaxation model is meaningful only if the variance is produced through turbulence, ie., $2\overline{\rho}\,\nu_t\left(\nabla\widetilde{c}\cdot\nabla\widetilde{c}\right)/Sc_t$ in Eq. (10), with no chemical reaction. This is acceptable for $\widetilde{\varepsilon}_\xi$ since $\widetilde{\xi}$ is a non-reacting scalar. The adequacy of the linear relaxation model for a passive scalar variance has been studied in the past, for example see [60]. The model in Eq. (11) satisfies the above requirement [49] and it reduces to the linear relaxation model outside the flammability limit since $s_L=0$ for non-flammable mixtures. Hence, it is inconsistent to ignore the contributions of combustion to $\widetilde{\varepsilon}_c$ while including them through the reaction terms for $\widetilde{c}$ and $\sigma^2_{c,\mathrm{sgs}}$.

It is equivalent to use either normalised, c, or unnormalised, ψ, progress variable in the combustion modelling but for the presumed PDF approach one must be cautious. The presumed Beta function requires its variable to be bounded between 0 and 1 and this is satisfied naturally by c. One can satisfy this for ψ by normalising it using ψ^{eq}, ie., $\psi_n=\psi/\psi^{eq}$, which is the same as c. This yields $0\leq\widetilde{c}$ or $\widetilde{\psi_n}\leq 1$ and there is no such bounds for $\widetilde{\psi}$ - the filtered quantity that will be transported in LES. One can ensure that the bounds are 0 and 1 using $\widetilde{\psi_n}=\widetilde{\psi}/\psi^{eq}$, which is acceptable only for fully premixed systems. The equilibrium value, ψ^{eq}, depends on the mixture fraction in partially premixed systems and thus $\widetilde{\psi_n}=\widetilde{(\psi/\psi^{eq})}\neq\widetilde{\psi}/\psi^{eq}$. Hence, it is better to use $\widetilde{c}$ to ensure physical and mathematical consistencies and also it allows us to separate premixed and

non-premixed contributions as in Eq. (6).

C. Numerical detail

The computational domain includes swirler, air passage, pre-chamber and the combustor volume (hot region) shown in Fig. 1a up to the end of the cylindrical section of diameter 50 mm. This domain was discretised in previous studies [5, 6] using a block-structured grid having 8.5 M hexahedral cells with refined grid in the flame region, pre-chamber and around the swirler walls. This numerical grid was shown to be good for LES in [5, 6], so it is used here for a comparative evaluation.

A pressure-based implicit splitting of operators (PISO) method [61] is used for the velocity-pressure-density coupling and a segregated solver is used for other equations. Second order central differencing schemes are used for spatial derivatives with a Gamma limiter for the velocity field and TVD limiters for the scalars to control numerical oscillations. Indeed, an overshoot less than 1% and an undershoot value larger than -0.01 was observed for $\widetilde{c}$ in various simulations reported here. An implicit Euler scheme is used for time derivatives since second order schemes were observed to be unstable in OpenFOAM unless a blending factor of the order of 0.3 was used [62]. The accuracy gain in using such second order scheme is observed to be not cost effective and thus a small time step of $\Delta t = 0.5$ μs is used for the Euler scheme to ensure good time accuracy. This gives a maximum CFL number of 0.07 and 0.1 for chamber and prechamber regions respectively (an average of about 0.35 for the entire computational domain). Moreover, 5 subiterations are performed for each time step to maintain close coupling among the various physical quantities as the simulations evolve. This iterative loop on the PISO algorithm is referred as "Pimple" algorithm in OpenFOAM. Additional simulations are performed using different NVD and TVD schemes available in OpenFOAM in combination with a blended second order temporal scheme and the results do not show significant differences. Thus, the numerical schemes, grid and Δt used are effective to ensure good accuracy and to avoid unphysical numerical oscillations.

Boundary conditions specified are as follows for well-posedness of the computational model [63, 64]. The combustor walls are treated to be adiabatic and no-slip with the two-layer wall model for the near-wall flows [65]. The vortex breakdown in swirling flows produces turbulence and thus the influences of the wall function and inlet turbulence (none specified) on the simulation results are

small. All the scalar variables are specified to have zero derivative in the wall normal direction. Dirichelet Boundary conditions are used for pressure at the outlet while velocity and scalars are updated from the solution using a zero-order extrapolation since the numerical schemes used is not one-sided [66]. At the inlet, Dirichelet conditions are imposed for velocity (in terms of mass flow rates) and all scalars except for the pressure, which is extrapolated from inside the domain. Diffusion fluxes are set to zero at the boundaries to respect the viscous condition [64]. The variables $\widetilde{c}$, k, σ_ξ^2 and $\sigma_{c,\mathrm{sgs}}^2$ are specified to be zero at the inlets and, $\widetilde{\xi} = 0$ and 1 are specified for the air and fuel inlets respectively. The enthalpies in various streams are specified to be consistent with their temperature and composition.

The simulations are run for about 50 ms of physical time and statistics are collected for the last 30 ms corresponding to about 7 flow-through times. The flow-through time of about 4.5 ms is defined based on the combustor length and bulk-mean velocity. Each simulation took about 1.5 days using 768 Intel Ivy Bridge cores on the ARCHER, UK national facility.

D. Flamelet table

The flamelet reaction rate, $\dot{\omega}(c, \xi)$, is obtained from unstrained planar laminar premixed flames with ξ spanning the entire flammability limits for the operating conditions of the SGT-100. The CH4-air mixture is flammable for $0.018 \leq \xi \leq 0.15$ ($0.31 \leq \phi \leq 1.9$) at $p = 3$ bar. These laminar flames are computed using PREMIX code [67], which solves conservation equations for mass, momentum, energy and species mass fractions with mixture-averaged transport properties for a freely propagating one-dimensional planar premixed laminar flame. Combustion chemistry is modelled using GRI-Mech 3.0 kinetics mechanism. The reactant mixture temperature is set according to its variation with the mixture fraction when the air is 685 K and the fuel is at 305 K as in the experiment. Typical variation of $\dot{\omega}$ with c and ξ is shown in Fig. 2 and the superscript + here and in the subsequent discussions implies that the quantities are appropriately normalised using $\delta_{th} = 0.19$ mm, $s_L = 0.66$ m/s, and unburnt mixture density of $\rho_u = 1.15$ kg/m^3 for the flamelet with $\xi = 0.034$. This mixture fraction corresponds to the overall equivalence ratio of the SGT-100 test condition studied here. The normalised reaction rate has a maximum of about 6.2 around the stoichiometry, $\xi_{\mathrm{st}} = 0.055$ and for $c \approx 0.8$. This reaction rate is integrated using Eq. (7) to get $\overline{\dot{\omega}}_{\mathrm{fp}}$

which is then tabulated as function of $\widetilde{c}$, $\sigma^2_{c,\mathrm{sgs}}$, $\widetilde{\xi}$, and $\sigma^2_{\xi,\mathrm{sgs}}$. The quantities $\widetilde{C}_p$, $\widetilde{\Delta h^0_f}$ and mixture molecular weight are computed following a similar procedure and are included in the look-up table. The filtered reaction rate is zero outside the flammability limits whereas the other quantities are linearly interpolated to the air and fuel values [41]. In addition to these quantities, values of s_L, δ_{th} and τ are also included as they are needed for Eq. (11). For the look-up table, uniformly spaced 100 and 50 points are used for $0 \leq \widetilde{c} \leq 1$ and $0 \leq \sigma^2_{c,\mathrm{sgs}} \leq \widetilde{c}\,(1-\widetilde{c})$ spaces respectively, and 200 points are used for $0 \leq \widetilde{\xi} \leq 1$. For the reasons discussed below, 15 points concentrated near 0 are used for $0 \leq \sigma^2_{\xi,\mathrm{sgs}} \leq \widetilde{\xi}\left(1-\widetilde{\xi}\right)$.

Typical variation of the filtered reaction rate with $\widetilde{c}$ and $\sigma^2_{c,\mathrm{sgs}}$ is shown in Fig. 3a for $\widetilde{\xi} = 0.034$ and $\sigma^2_{\xi,\mathrm{sgs}} = 0$. This variation is similar for other $\widetilde{\xi}$ values except for the magnitude of $\overline{\dot{\omega}}_{\mathrm{fp}}$. The peak value at $\widetilde{c} \approx 0.8$ drops from 2.3 for $\sigma^2_{c,\mathrm{sgs}} = 0$ to about 50% smaller value for $\sigma^2_{c,\mathrm{sgs}} = 0.05$. The reaction rate variation in $\widetilde{c} - \widetilde{\xi}$ space has a peak at $c \approx 0.8$, as for the flamelets shown in Fig. 2, for all flammable mixture fraction when $\sigma^2_{c,\mathrm{sgs}} = 0$. This peak spreads in the $\widetilde{c}$ space and its magnitude reduces as $\sigma^2_{c,\mathrm{sgs}}$ increases for a given value of $\widetilde{\xi}$ as shown in Fig. 3a.

1. Effect of SGS variance

The typical influence of $\sigma^2_{\xi,\mathrm{sgs}}$ on $\overline{\dot{\omega}}_{\mathrm{fp}}$ is shown in Fig. 3b for $\widetilde{\xi} = 0.034$, $\widetilde{c} = 0.5$ and three values of $\sigma^2_{c,\mathrm{sgs}}$. Increasing $\sigma^2_{\xi,\mathrm{sgs}}$ produces a sharp increase in the filtered reaction rate for $\sigma^2_{\xi,\mathrm{sgs}} < 0.001$ followed by a gradual decrease. This increase is amplified for $\sigma^2_{c,\mathrm{sgs}} \leq 0.1$ as shown in the figure suggesting that the effect of $\sigma^2_{\xi,\mathrm{sgs}}$ is quite non-linear. The maximum total (resolved + SGS) variance observed in the experiment [19] is about 1×10^{-4} and thus the corresponding SGS variance can be expected to be smaller than this value. Because of the non-linearity observed in Fig. 3b, one cannot ignore this variance. Hence three different scenarios are considered for LES to investigate this systematically as listed in Table 1. The first case assumes that $\sigma^2_{\xi,\mathrm{sgs}} = 0$ and $\overline{\dot{\omega}}_{\mathrm{np}} = 0$ implying that the combustion is stratified and each mixture burns in premixed mode, which simply means that $\overline{\dot{\omega}}_{\mathrm{fp}} = \int \dot{\omega}(\zeta,\ \eta = \widetilde{\xi})\ P(\zeta)\ \mathrm{d}\zeta$ from Eq. (7). This scenario is referred as Case A in the table and subsequent discussion. In Case B, the non-premixed contribution is included with $\sigma^2_{\xi,\mathrm{sgs}} = 0$. This helps us to investigate the influence of non-premixed mode on the flow and flame statistics. Case C

considers the mixture fraction variance through its transport equation and includes non-premixed mode also and thus it is the case of partially premixed combustion. Results from these simulations are presented and discussed next.

Table 1: Three scenarios considered for LES

Case	$\overline{\dot{\omega}}_{\rm np}$	$\sigma^2_{\xi,\rm sgs}$	$P(\psi)$
A	0	0	$\delta(\eta - \widetilde{\xi})$
B	Eq. (8)	0	$\delta(\eta - \widetilde{\xi})$
C	"	Eq. (9)	$\beta(\eta;\, \widetilde{\xi}, \sigma^2_{\xi,\rm sgs})$

IV. Results

The spatial variation of time-averaged resolved turbulent kinetic energy computed as $\langle \mathcal{K} \rangle_{\rm res} = 0.5[\langle \widetilde{U}_i \widetilde{U}_i \rangle - \langle \widetilde{U}_i \rangle \langle \widetilde{U}_i \rangle]$, is shown in Fig. 4 for the mid-plane through the computational domain. The symbol $\langle \Phi \rangle$ is used for both Reynolds and Favre averages and this depends on whether the quantity Φ is Reynolds or Favre filtered. The large value of $\mathcal{K}$ along the centreline in downstream locations is due to the central vortex core (CVC) arising from the swirling flow. The shear layer between the CVC and the central recirculation zone (CRZ) produces considerably large $\mathcal{K}$ around $x \approx 120\,$mm and $y \approx \pm 30\,$mm. The variation of an intermediate value of $\mathcal{K} \approx 200$ shows the shape and size of the CRZ and it is apparent that it fills the entire combustor width. A detailed analysis of $\mathcal{Q} = k/(k + \mathcal{K})$ showed that the SGS kinetic energy, k, is below 20% everywhere in the domain. Thus, the numerical grid used is very good as noted in earlier LES studies employing this grid. The 20% criterion introduced by Pope [31] was for non-reacting flows and one must be mindful of dominant heat release effects in reacting flows with low turbulence [68]. This is not the case for the conditions of the SGT-100 and so this criterion works quite well. Also, this grid resolves the mixture fraction field well (see section IV C) and so the mean of the residual field is $\langle \Phi" \rangle \simeq 0$ and hence $\langle \widetilde{\Phi} \rangle \simeq \langle \Phi \rangle$ [69]. Hence the tilde notation will be dropped in the following discussion for the sake of simplicity.

A. General flow features

Figure 5 illustrates typical flow structures using vorticity iso-surfaces (15000 s^{-1}) coloured by temperature and pressure iso-surface coloured by vorticity. The intense vortical structures are concentrated in the CRZ except for the CVC. The largest vortices in the compact CRZ stabilise the flame (see next subsection), and specifically, the inner recirculation zone attached to the burner's rear surface provides the strongest anchoring mechanism [21]. The hot gases accelerate in the converging section causing the pressure iso-surface of 300.6 kPa to expand. This generates a strong CVC extending to the outlet. The vorticity colours on the pressure iso-surface demonstrates that the vorticity level drops significantly because of flow acceleration. The highest vorticity in the CVC in the downstream region is about 7000 s^{-1}. From this picture, it is quite clear that the flow structures are complex and highly turbulent and these gross features do not vary unduly for the 3 cases listed in the table 1.

The measured and computed CRZ structures are compared in Fig. 6 using planar velocity magnitude and its streamlines in the mid-plane. The computational results are shown for Cases B and C, and this result for Case A is similar to that shown for the Case B. Two large vortices are formed on either side of the centreline confined by the expanding reactant jets exiting the pre-chamber. The outer recirculation zone (ORZ) resulting from the sudden expansion of the prechamber is also evident. The CRZ size and shape were noted to be influenced by its interaction with the CVC [5] and chemical kinetics mechanism used for combustion chemistry [6]. The differences in the streamline pattern between Cases B and C support this as the heat release is influenced by the choice of the combustion closure, either B or C, which would affect the local density and flow. The flow pattern of time-averaged velocities is expected to be symmetric about the centerline which is observed for Case C. The rear stagnation point, marked using a circle, is near the centreline for Case C, which is not so for Case B. Also, the results in Fig. 6b suggest that the reactant jet from the prechamber spreads quickly in the radial direction in Case B resulting in reduced jet penetration. This causes the rear stagnation point to shift upstream. The measured asymmetric streamline pattern in Fig. 6a suggests that the stagnation point is located at about $x \simeq 150$ and $r \simeq -25$. This off-centre location implies the presence of precessing CVC, also noted in [21], and

possibly its bias on the measured statistics because the data may not have been collected for a long enough period. This observation is supported by the measured radial velocity $\langle V \rangle \neq 0$ along the centreline (discussed below). Overall, the flow pattern and reactant jet penetration agree quite well for Case C. However, a close scrutiny of the results in this figure suggests that the radial expansion of the reactant jet is under estimated in Case C – compare the region with the maximum velocity magnitude for $x \geq 50$ mm in Figs. 6a and 6c – which would reflect in the velocity comparisons to be shown next.

Figures 7 and 8 compare measured (Favre-averaged) statistics of axial and radial velocities with those computed here and the radial, r, variations are shown for 4 axial locations marked in Fig. 1. The time-averaged radial variation is also averaged azimuthally and thus $r = 0$ corresponds to $y = 0$ in Fig. 6. The mean velocities are predicted quite well by all the three models. However, the computed rms values show larger deviation from the experimental data as in figures 7 and 8, which may be due to the influence of mixture fraction fluctuations and non-premixed combustion. There is some difference between measured and computed $\langle U \rangle$ for Loc. 3 and 4, and also the negative $\langle U \rangle$ along the centreline is over estimated for Loc. 1 and 2. These are related to the under estimate of the jet expansion noted earlier. The location of peak $\langle V \rangle$ is captured in the LES but there is some under-prediction of $\langle V \rangle$ and $V_{\rm rms}$ for $r > 50\,$mm at downstream locations. It is worth to note that $\langle V \rangle = 0$ at $r = 0$ in the LES results, which is not so in the measurements for the reasons noted above. Overall, these comparisons are similar to those observed in earlier studies as shown in the Appendix.

B. General flame features

Figure 9a shows an instantaneous snapshot of OH-PLIF coloured using OH gradient estimated using the PLIF image. It is quite clear that an 'M' shaped flame is established at the prechamber exit by the toroidal vortex in the CRZ and its interaction with the reactant jet issuing from the prechamber. The bottom half of the flame is relatively fainter because of the energy attenuation in the laser sheet coming from the top side. The wrinkling caused by the turbulence is also evident in this instantaneous image. If one apply LES filtering then these wrinkling will be smeared depending on the filter size.

The flame computed for Cases B and C at an arbitrary time is also shown in Fig. 9 . Case A is not shown here because the spatial variation of $\overline{\dot{\omega}}^*$ is very similar to that shown for Case B. This is because the non-premixed mode, $\overline{\dot{\omega}}^+_{\rm np}$, contribution is relatively small as one shall observe later (in Fig. 10). Thus, the differences observed between Cases B and C are because $\sigma^2_{\xi,\rm sgs} \neq 0$ in Case C. This variance affects the magnitude of the reaction rate substantially and thus the flame shape. The SGS fluctuation of the mixture fraction allows leaner and richer mixtures into the local numerical cell and their relative amount depends on the value of $\widetilde{\xi}$ in that cell and thus the filtered reaction rate can either increase or decrease if one includes $\sigma^2_{\xi,\rm sgs}$. A careful comparison of Figs. 9b and 9c shows this clearly and a good comparison for the flame shape and location is observed between the measurements and Case C. The fine scale wrinkling seen in the measurements can only be captured in LES if (direct numerical simulation) DNS-like numerical resolution is used, which is not the objective of this study. Thus, Fig. 9a should not be compared to the LES results directly. However, this comparison helps to understand the LES and its modelling in capturing general features such as flame shape and position qualitatively.

Figure 10 compares the contribution of $\overline{\dot{\omega}}^+_{\rm np}$ to the total normalised reaction rate $\overline{\dot{\omega}}^*$. The contribution of $\overline{\dot{\omega}}^+_{\rm np}$ is two orders of magnitude smaller than $\overline{\dot{\omega}}^*$ and it occurs only in the lip region of the prechamber having stoichiometric mixture fraction and non-zero $\widetilde{c}$ (see Eq. 8). A predominant influence of this mode is seen only for the outer branches of the 'M' flame and thus combustion in the SGT-100 occurs mostly in stratified premixed mode, which is consistent with the analysis in [21]. However, a strong non-premixed mode is not observed in the prechamber region here unlike in [21]. The combustion occurs in both the inner and outer shear layers. The flame is anchored by the strong reaction rate near the prechamber lip (see Fig. 10a), and in the inner recirculation region. The later is observed to be a stronger flame stabilisation mechanism compared to the former, which is similar to that reported in [21].

C. Comparison of mixture fraction statistics

The computed radial variations of mean and rms of the mixture fraction are compared to measurements in Fig. 11. The results are shown for four axial locations and for all three cases listed in Table 1. The experimental studies [6, 19] reported Favre-averaged statistics and thus these

values computed using their respective transport equations are compared directly. The rms value is obtained from the total variance $\sigma_\xi^2 \approx \langle \xi^2 - \langle \xi \rangle^2 \rangle + \langle \sigma_{\xi,\mathrm{sgs}}^2 \rangle$, which is the sum of resolved and SGS variances, since it is assumed that the average of the residual is zero, $\langle \xi" \rangle \simeq 0$ [69, 70]. A good agreement between the measured and computed $\langle \xi \rangle$ is observed, except for an over estimate of the peak value at Loc. 1. This over-prediction is because of under estimate of the reactant jet penetration noted in Fig. 6 since the mixture fraction is a passive scalar and so its variation is dictated by the flow field.

The agreement between measured and computed $\langle \xi \rangle$ becomes very good as one moves downstream and this is similar to those observed in earlier studies (see the Appendix). The measured variation along the centreline is also captured well in the LES. The experimental data suggests that $\langle \xi \rangle$ along the centreline increases gradually from 0.029 at Loc. 1 to 0.031 at Loc. 4 and also the fully mixed value of 0.034 corresponding to the inlet air and fuel flow rates is not observed in the measurements. This suggests that the CRZ is leaner (lower $\langle \xi \rangle$), and richer mixture fraction values are observed for radial positions of $r > 50$ mm as suggested by the LES results and these positions are not covered in the experiments. The measurements suggest that the CVC has homogeneous mixture fraction which is also captured in the LES (see Fig. 12 also). The small difference observed among the three cases suggests that the averaged mixture fraction value is not sensitive to $\sigma_{\xi,\mathrm{sgs}}^2$ or $\overline{\dot{\omega}}_{\mathrm{np}}$ as this contribution was found to be small compared to $\overline{\dot{\omega}}_{\mathrm{fp}}$ in Fig. 10. However, the rms of mixture fraction is observed to have some small sensitivity as seen in Fig. 11. The computed σ_ξ agrees quite well with the measurements and the centreline value is slightly under estimated. The peak rms is about 1×10^{-2}, which is about 5% of the maximum possible value of $\sqrt{\langle \xi \rangle (1 - \langle \xi \rangle)} \approx 0.183$ at $r = 40$ mm for the first axial location. It is worth to note that the rms values shown in the figures include only the resolved part because $\sigma_{\xi,\mathrm{sgs}}^2 = 0$ for the Cases A and B, and so the SGS part was excluded for the Case C to be consistent. The good agreement seen here suggests that the mixture fraction fluctuations are resolved quite well by the numerical grid used here and the SGS rms value is small. This is confirmed in Fig. 12 showing the spatial variations of $\widetilde{\xi}$ and $\sigma_{\xi,\mathrm{sgs}}^2$ in the mid-plane for Case C. This result is shown for the same time as that for Fig. 9. The flame region is marked using iso-lines of $\widetilde{c} = 0.05$ and 0.95. The CVC has mostly homogeneous mixture fraction confirming the

earlier observation and there is mixture stratification inside the flame marked using the iso-lines. The inner branch of the 'M' flame has leaner mixture while the outer branch experiences richer mixture. The burning rate in these flames are influenced by $\sigma^2_{\xi,\mathrm{sgs}}$ and thus one would expect to see substantial difference in the statistics of reactive scalars such as temperature and scalar mass fractions.

D. Temperature statistics

The radial variations of averaged temperature and its rms are shown in Fig. 13 for 4 axial locations. The results are shown for the three cases along with measured values. The rms, $\sigma_T \approx \sqrt{\langle T^2 - \langle T \rangle^2 \rangle}$, excludes the subgrid contribution and its effect is evaluated systematically below. The centreline variations of both $\langle T \rangle$ and σ_T are captured well in all three cases. The results for Cases A and B are almost the same since the non-premixed mode contribution is small and the SGS mixture fraction fluctuation is excluded. The averaged burnt temperature near the centreline is over estimated by about 100 K in these two cases and including $\sigma^2_{\xi,\mathrm{sgs}}$ in Case C improves this estimate as seen in the figure. However, the minimum averaged temperature computed is about 900 K for Loc. 1 while the measured value is about 690 K at $r \approx 42.5$ mm. A substantial improvement is observed for Case C compared to the other two cases and an over estimate of about 210 K is because of the under prediction of the jet expansion and penetration resulting in over prediction of the mixture fraction as noted in figures 6 and 11. Moreover, the fluid strain was observed to be highly intermittent, sometimes in excess of the extinction rate for the GRI 3.0 mechanism [21] and these excessive strain rates cause local quenching which decreases the average temperature. These may not be fully captured in the present study and requires further studies to assess strain effects. However, the over estimate of the minimum averaged temperature is similar to those observed in past studies as noted in the Appendix.

The computed σ_T agrees quite well with measurements, specifically along the centreline. Also, the values computed using the Cases A and B compare well with measurements whereas some under prediction is seen for the Case C in the flame region, $20 \leq r \leq 50$ mm. This under prediction is large for Loc. 1 and it improves as one moves downstream. This is because the SGS contribution, which can be substantial in flame region, is excluded. Some understanding of this contribution can

be obtained by estimating it in the following manner. If one defines a normalised temperature as $T^+ = (T - T_u)/(T_b - T_u)$ then the variance of this field can be related to σ_c^2 and thus $\sigma^2_{T^+,\mathrm{sgs}} \approx \sigma^2_{c,\mathrm{sgs}}$. This is strictly valid for fully premixed system with Lewis number close to unity [64]. For partially premixed combustion, both T_u and T_b depends on mixture fraction and also the Lewis number can vary spatially and thus the above approximation is less likely to hold. Nevertheless, one can gain some understanding from this. The total temperature variance obtained by adding the SGS and resolved variances is shown in Fig. 13 as dotted lines. There is a general overestimate confirming that the above approach of getting the subgrid variance is too crude. One can also use flamelet approximation to get the variance as $\widehat{\sigma}^2_{T,\mathrm{sgs}} = \int\int \left(T(\zeta,\,\eta) - \widetilde{T}\right)^2 P(\zeta,\,\eta)\;\; d\zeta\;\, d\eta$, where P is the SGS pdf as in Eq. (7). The total variance obtained using $\widehat{\sigma}^2_{T,\mathrm{sgs}}$ (not shown here) is very close to that calculated using $\sigma^2_{T^+,\mathrm{sgs}}$ noted above. Hence, it is quite clear that $\sigma^2_{T,\mathrm{sgs}}$ cannot be excluded and one may have to transport $\sigma^2_{T^+,\mathrm{sgs}}$ in the LES. This would require further modelling, which is not the focus of this study. However, a careful scrutiny of the temperature rms depicted in Fig. 13 shows the sensitivity of this quantity to mixture fraction fluctuation and partially premixed combustion modelling. A cross comparison with past studies is discussed in the Appendix.

E. Mass fraction comparison

The time-averaged species mass fractions are calculated in a post-processing step using

$$\langle \overline{Y} \rangle = \int_0^1 \int_0^1 Y(\zeta,\eta)\; P(\zeta,\eta) \quad \mathrm{d}\eta \;\; \mathrm{d}\zeta \tag{13}$$

which is similar to Eq. (7), but the joint PDF in the above equation is for time-averaged values of $\langle \widetilde{c} \rangle$ and $\langle \widetilde{\xi} \rangle$, and total variances σ_c^2 and σ_ξ^2 which include resolved and SGS variance. Hence, this is not the SGS PDF and it is followed here based on earlier study [28]. Radial variations of species mass fractions computed thus are compared to measurements in Figs. 14 and 15 for the 4 axial locations. The computational results are shown for all the three cases and the small differences observed between the Cases A and B are because the contribution of non-premixed mode combustion is small and the absence of SGS mixture fraction fluctuation. Significant improvement is observed when this fluctuation is included in the modelling, which is consistent with the temperature comparisons shown earlier. However, the under estimate of CH4 and O2 are consistent with the over estimate of

CO2 and H2O mass fractions in the flame region and these are related to the under prediction of the jet expansion and penetration noted earlier. The comparison between measured and computed mass fractions improve considerably as one moves downstream for Case C. Furthermore, these comparisons are comparable to those observed in past studies, see Appendix.

V. Concluding Remarks

The reacting flow in the SGT-100 combustor is simulated using LES involving premixed flamelets as SGS closure for the filtered reaction rate. The flamelets ranging from lean to rich flammability limits are used along with a simple model involving total (resolved + SGS) scalar dissipation rate of mixture fraction, see Eq. (8), for non-premixed combustion around stoichiometric mixture fraction. The filtered reaction rates obtained using these flamelets are tabulated with filtered progress variable, mixture fraction and their respective SGS variances as controlling variables, which are transported in the LES. The mixture fraction SGS dissipation rate is modelled using a linear relaxation model whereas an algebraic model is used for progress variable dissipation rate to include contributions from combustion and turbulence. This algebraic model maintains physical consistencies as discussed in section III B 1. The influences of SGS mixture fraction fluctuation and non-premixed mode combustion on the computed statistics are evaluated systematically and these statistics are compared to measurements.

The predicted size and shape of the CRZ compare quite well with those obtained from PIV and this comparison is similar to those in past studies (see Appendix). Comparison of the filtered heat release rate with OH PLIF demonstrates that the LES model used here captures the M-shaped flame stabilised in the shear layer regions surrounding the CRZ and ORZ as observed in the experiments. However, the outer branch of the flame is seen to have a relatively increased heat release rate leading to under estimate of the reactant jet penetration and expansion inside the combustor. The contribution of non-premixed combustion is observed to be small compared to the total reaction rate in partially premixed combustion occurring inside the SGT-100. The SGS mixture fraction variance influences the reaction rate and thus the statistics of temperature and major species mass fractions. The agreement with the measurements improves substantially when reaction rate of partially premixed combustion is modelled using contributions from premixed and non-premixed

modes including the effects of SGS mixture fraction variance. The predominant effect is observed to come from this variance. However, some over-prediction of mixture fraction is observed which may be related to the under prediction of reactant jet penetration inside the combustor. Avenues to improve this by including the SGS flame stretch or SGS correlation between the mixture fraction and progress variable will be explored in future since the filter width implied by the grid suggests that these residual effects may not be small. The strained flamelets [49] or copula [41, 43] methodology could be used to capture these effects.

Acknowledgements

This work is funded by EPSRC project number EP/I027556/1. Access to the ARCHER supercomputer provided by the UK Research Data Facility (http://www.archer.ac.uk/documentation/rdf-guide) and UKCTRF are gratefully acknowledged.

[1] Hassa, C., "Partially Premixed and Premixed Aeroengine Combustors," *Gas Turbine Emissions*, edited by T. C. Lieuwen and V. Yang, Cambridge University Press, Cambridge, 2013, pp. 237–289.

[2] Masri, A. R., "Partial Premixing and Stratification in Turbulent Flames," *Proceedings of the Combustion Institute*, Vol. 35, No. 2, 2015, pp. 1115–1136. doi:10.1016/j.proci.2014.08.032.

[3] Pitsch, H., "Large-Eddy Simulation of Turbulent Combustion," *Annual Reviews of Fluid Mechanics*, Vol. 38, Jan. 2006, pp. 453–482. doi:10.1146/anurev.fluid.38.050304.092133.

[4] Gicquel, L. Y. M., Staffelbach, G., and Poinsot, T., "Large Eddy Simulations of Gaseous Flames in Gas Turbine Combustion Chambers," *Progress in Energy and Combustion Science*, Vol. 38, No. 6, 2012, pp. 782–817. doi:10.1016/j.pecs.2012.04.004.

[5] Bulat, G., Jones, W. P., and Marquis, A. J., "NO and CO Formation in an Industrial Gas-Turbine Combustion Chamber Using LES with the Eulerian Sub-Grid PDF Method," *Combustion and Flame*, Vol. 161, No. 7, 2014, pp. 1804–1825. doi:10.1016/j.combustflame.2013.12.028.

[6] Bulat, G., Fedina, E., Fureby, C., Meier, W., and Stopper, U., "Reacting Flow in an Industrial Gas Turbine Combustor: LES and Experimental Analysis," *Proceedings of the Combustion Institute*, Vol. 35, No. 3, 2015, pp. 3175–3183. doi:10.1016/j.proci.2014.05.015.

[7] Abou-Taouk, A., Farcy, B., Domingo, P., Vervisch, L., Sadasivuni, S., and Eriksson, L. E., "Optimized Reduced Chemistry and Molecular Transport for Large Eddy Simulation of Partially Premixed Combustion in a Gas Turbine," *Combustion Science and Technology*, Vol. 188, No. 1, 2016, pp. 21–39.

doi:10.1080/00102202.2015.1074574.

[8] Charlette, F., Meneveau, C., and Veynante, D., "A Power-Law Flame Wrinkling Model for LES of Premixed Turbulent Combustion, Part I: Non-Dynamic Formulation and Initial Tests," *Combustion and Flame*, Vol. 131, No. 1–2, 2002, pp. 159–180. doi:10.1016/S0010–2180(02)00400–5.

[9] Wang, G., Boileau, M., and Veynante, D., "Implementation of a Dynamic Thickened Flame Model for Large Eddy Simulations of Turbulent Premixed Combustion," *Combustion and Flame*, Vol. 158, No. 11, 2011, pp. 2199–2213. doi:1016/j.combustflame.2011.04.008.

[10] Srinivasan, S., Ranjan, R., and Menon, S., "Flame Dynamics During Combustion Instability in a High-Pressure, Shear-Coaxial Injector Combustor," *Flow Turbulence and Combustion*, Vol. 94, No. 1, 2015, pp. 237–262. doi:10.1007/s10494–014–9569–x.

[11] Fureby, C., "A Fractal Flame-Wrinkling Large Eddy Simulation Model for Premixed Turbulent Combustion," *Proceedings of the Combustion Institute*, Vol. 30, No. 1, 2005, pp. 593–601. doi:10.1016/j.proci.2004.08.068.

[12] Sabelnikov, V. and Fureby, C., "LES Combustion Modeling for High Re Flames Using a Multi-Phase Analogy," *Combustion and Flame*, Vol. 160, No. 1, 2013, pp. 83–96. doi:10.1016/j.combustflame.2012.09.008.

[13] Jones, W. P., Marquis, A. J., and Prasad, V. N., "LES of a Turbulent Premixed Swirl Burner Using the Eulerian Stochastic Field Method," *Combustion and Flame*, Vol. 159, No. 10, 2012, pp. 3079–3095. doi:10.1016/j.combustflame.2012.04.008.

[14] Dunstan, T. D., Minamoto, Y., Chakraborty, N., and Swaminathan, N., "Scalar Dissipation Rate Modelling for Large Eddy Simulation of Turbulent Premixed Flames," *Proceedings of the Combustion Institute*, Vol. 34, No. 1, 2013, pp. 1193–1201. doi:10.1016/j.proci.2012.06.143.

[15] Butz, D., Gao, Y., Kempf, A. M., and Chakraborty, N., "Large Eddy Simulations of a Turbulent Premixed Swirl Flame Using an Algebraic Scalar Dissipation Rate Closure," *Combustion and Flame*, Vol. 162, No. 9, 2015, pp. 3180–3196. doi:10.1016/j.combustflame.2015.05.003.

[16] Sadasivuni, S. K., Bulat, G., Sanderson, V., and Swaminathan, N., "Application of Scalar Dissipation Rate Model to Siemens DLE Combustors," *ASME Turbo Expo: Turbine Technical Conference and Exposition*, American Soc. of Mechanical Engineers GT2012-68483, Copenaghen, 2012.

[17] Ruan, S., Swaminathan, N., Isono, M., Saitoh, T., and Saitoh, K., "Simulation of Premixed Combustion with Varying Equivalence Ratio in Gas Turbine Combustor," *Journal of Propulsion and Power*, Vol. 31, No. 3, 2015, pp. 861–871. doi:10.2514/1.B35517.

[18] Kohse-Höinghaus, K., Barlow, R. S., Aldén, M., and Wolfrum, J., "Combustion at the Focus: Laser Diagnostics and Control," *Proceedings of the Combustion Institute*, Vol. 30, No. 1, 2005, pp. 89–123. doi:10.1016/j.proci.2004.08.274.

[19] Stopper, U., Meier, W., Sadanandan, S., Stör, M., Aigner, M., and Bulat, G., "Experimental Study of Industrial Gas Turbine Flames Including Quantification of Pressure Influence on Flow Field, Fuel/Air Premixing and Flame Shape," *Combustion and Flame*, Vol. 160, No. 10, 2013, pp. 2103–2118. doi:10.1016/j.combustflame.2013.04.005.

[20] Jaravel, T., Riber, E., Cuenot, B., and Bulat, G., "Large Eddy Simulation of an Industrial Gas Turbine Combustor Using Reduced Chemistry with Accurate Pollutant Prediction," *Proceedings of the Combustion Institute*, Vol. 36, No. 3, 2017, pp. 3817–3825.doi:10.1016/j.proci.2016.07.027.

[21] Fedina, E., Fureby, C., Bulat, G., and Meier, W., "Assessment of Finite Rate Chemistry Large Eddy Simulation Combustion Models," *Flow Turbulence and Combustion*, Vol. 99, No. 2, 2017, pp. 385–409. doi:10.1007/s10494–017–9823–0.

[22] Roberts, W. L., Driscoll, J. F., Drake, M. C., and Goss, L. P., "Images of the Quenching of a Flame by a Vortex—to Quantify Regimes of Turbulent Combustion," *Combustion and Flame*, Vol. 94, No. 1–2, 1993, pp. 58–69. doi:10.1016/0010–2180(93)90019–Y.

[23] Dunn, M. J., Masri, A. R., and Bilger, R. W., "A New Piloted Premixed Jet Burner to Study Strong Finite-Rate Chemistry Effects," *Combustion and Flame*, Vol. 151, No. 1–2, 2007, pp. 46–60. doi:10.1016/j.combustflame.2007.05.010.

[24] Dunn, M. J., Masri, A. R., Bilger, R. W., Barlow, R. S., and Wang, G. H., "The Compositional Structure of Highly Turbulent Piloted Premixed Flames Issuing into a Hot Coflow," *Proceedings of the Combustion Institute*, Vol. 32, No. 2, 2009, pp. 1779–1786. doi:10.1016/j.proci.2008.08.007.

[25] Meneveau, C. and Poinsot, T., "Stretching and Quenching of Flamelets in Premixed Turbulent Combustion," *Combustion and Flame*, Vol. 86, No. 4, 1991, pp. 311–332. doi:10.1016/0010–2180(91)90126–V.

[26] Knudsen, E. and Pitsch, H., "Capabilities and Limitations of Multi-Regime Flamelet Combustion Models," *Combustion and Flame*, Vol. 159, No. 1, 2012, pp. 242–264. doi:10.1016/j.combustflame.2011.05.025.

[27] Srinivasan, S. and Menon, S., "Linear Eddy Mixing Model Studies of High Karlovitz Number Turbulent Premixed Flames," *Flow Turbulence and Combustion*, Vol. 93, No. 2, 2014, pp. 189–219. doi:10.1007/s10494–014–9542–8.

[28] Langella, I., Swaminathan, N., and Pitz, R. W., "Application of Unstrained Flamelet SGS Closure for Multi-Regime Premixed Combustion," *Combustion and Flame*, Vol. 173, Nov. 2016, pp. 161–178.

doi:10.1016/j.combustflame.2016.08.025.

[29] Peters, N., *Turbulent Combustion*, Cambridge University Press, 2000.

[30] Weller, H. G., Tabor, G., Jasak, H., and Fureby, C., "A Tensorial Approach to Computational Continuum Mechanics Using Object-Oriented Techniques," *Computers in Physics*, Vol. 12, No. 6, 1998, pp. 620–631. doi:10.1063/1.168744.

[31] Pope, S. B., "Large-Eddy Simulation," *Turbulent Flows*, chap. 13, Cambridge University Press, Cambridge, 2000.

[32] Chai, X. and Mahesh, K., "Dynamic k-Equation Model for Large Eddy Simulation of Compressible Flow," *Journal of Fluid Mechanics*, Vol. 699, Apr. 2012, pp. 385–413. doi:10.1017/jfm.2012.115.

[33] Langella, I., Swaminathan, N., Gao, Y., and Chakraborty, N., "LES of Premixed Combustion: Sensitivity to SGS Velocity Modelling," *Combustion Science and Technology*, Vol. 189, No. 1, 2017, pp. 43–78. doi:10.1080/00102202.2016.1193496.

[34] Bilger, R. W., Stårner, S. H., and Kee, R. J., "On Reduced Mechanism for Methane-Air Combustion in Nonpremixed Flames," *Combustion and Flame*, Vol. 80, 1990, pp. 135–149. doi:10.1016/0010–2180(90)90122–8.

[35] Chen, Z., Ruan, S., and Swaminathan, N., "Large Eddy Simulation of Flame Edge Evolution in a Spark-Ignited Methane-Air Jet," *Proceedings of the Combustion Institute*, Vol. 36, 2017, pp. 1645–1652. doi:10.1016/j.proci.2016.06.023.

[36] Ihme, M., Shunn, L., and Zhang, J., "Regularization of reaction progress variable for application to flamelet-based combustion models," *Journal of Computational Physics*, Vol. 231, No. 23, 2012, pp. 7715–7721. doi:10.1016/j.jcp.2012.06.029.

[37] Fiorina, B., Baron, R., Gicquel, O., Thevenin, D., Carpentier, S., and Darabiha, N., "Modelling Non-Adiabatic Partially Premixed Flames Using Flame-Prolongation of ILDM," *Combustion Theory and Modelling*, Vol. 7, No. 3, 2003, pp. 449–470. doi:10.1088/1364–7830/7/3/301.

[38] Bray, K. N. C., Domingo, P., and Vervisch, L., "Role of the Progress Variable in Models for Partially Premixed Turbulent Combustion," *Combustion and Flame*, Vol. 141, 2005, pp. 431–437. doi:10.1016/j.combustflame.2005.01.017.

[39] Ruan, S., Swaminathan, N., Bray, K. N. C., Mizobuchi, Y., and Takeno, T., "Scalar and its Dissipation in the Near Field of Turbulent Lifted Jet Flame," *Combustion and Flame*, Vol. 159, 2012, pp. 591–608. doi:10.1016/j.combustflame.2011.07.014.

[40] Domingo, P., Vervisch, L., and Réveillon, J., "DNS Analysis of Partially Premixed Combustion in Spray and Gaseous Turbulent Flame-bases Stabilized in Hot Air," *Combustion and Flame*, Vol. 140, 2005,

pp. 172–195. doi:10.1016/j.combustflame.2004.11.006.

[41] Ruan, S., Swaminathan, N., and Darbyshire, O., "Modelling of Turbulent Lifted Jet Flames Using Flamelets: *a Priori* Assessment and *a Posteriori* Validation," *Combustion Theory and Modelling*, Vol. 18, No. 2, 2014, pp. 295–329. doi:10.1080/13647830.2014.898409.

[42] Chen, Z., Ruan, S., and Swaminathan, N., "Simulation of Turbulent Lifted Methane Jet Flames: Effects of Air-Dilution and Transient Flame Propagation," *Combustion and Flame*, Vol. 162, No. 3, 2015, pp. 703–716. doi:10.1016/j.combustflame.2014.09.010.

[43] Darbyshire, O. and Swaminathan, N., "A Presumed Joint pdf Model for Turbulent Combustion with Varying Equivalence Ratio," *Combustion Science and Technology*, Vol. 184, No. 12, 2012, pp. 2036–2067. doi:10.1080/00102202.2012.696566.

[44] Pierce, C. D. and Moin, P., "Progress-variable Approach for Large-Eddy Simulation of Non-Premixed Turbulent Combustion," *Journal of Fluid Mechanics*, Vol. 504, 2004, pp. 73–97. doi:10.1017/S0022112004008213.

[45] Bilger, R. W., "The structure of diffusion flames," *Combustion Science and Technology*, Vol. 13, No. 1-6, 1976, pp. 155–170.doi:10.1080/00102207608946733.

[46] Bilger, R. W., "Future in turbulent combustion research," *Progress in Energy and Combustion Science*, Vol. 26, No. 4-6, 2000, pp. 367–380. doi:10.1016/S0360–1285(00)00015–0.

[47] Davis, P. J., "Gamma functions and related functions," *Handbook of mathematical functions*, edited by M. Abramowitz and I. A. Stegun, Dover Publications Inc., New York, 1970.

[48] Langella, I., Swaminathan, N., Williams, F. A., and Furukawa, J., "Large-Eddy Simulation of Premixed Combustion in the Corrugated-Flamelet Regime," *Combustion Science and Technology*, Vol. 188, No. 9, 2016, pp. 1565–1591. doi:10.1080/00102202.2016.1195824.

[49] Langella, I. and Swaminathan, N., "Unstrained and Strained Flamelets for LES of Premixed Combustion," *Combustion Theory and Modelling*, Vol. 20, No. 3, 2015, pp. 410–440. doi:10.1080/13647830.2016.1140230.

[50] Langella, I., Swaminathan, N., Gao, Y., and Chakraborty, N., "Assessment of Dynamic Closure for Premixed Combustion LES," *Combustion Theory and Modelling*, Vol. 19, No. 5, 2015, pp. 628–656. doi:10.1080/13647830.2015.1080387.

[51] Chakraborty, N., Champion, M., Mura, A., and Swaminathan, N., "Scalar-Dissipation-Rate Approach," *Turbulent Premixed Flames*, edited by N. Swaminathan and K. N. C. Bray, chap. 2.3, Cambridge University Press, 2011, pp. 74–102.

[52] Borghi, R. and Dutoya, D., "On the scales of the fluctuations in turbulent combustion," *Symposium (International) on Combustion*, Vol. 170, No. 1, 1979, pp. 235–244. doi:10.1016/S0082–0784(79)80025–9.

[53] Borghi, R., "Turbulent premixed combustion: Further discussions on the scales of fluctuations," *Combust. Flame*, Vol. 80, No. 304-312, 1990.

[54] Mantel, T. and Borghi, R., "A New Model of Premixed Wrinkled Flame Propagation Based on a Scalar Dissipation Equation," *Combustion and Flame*, Vol. 96, No. 4, 1994, pp. 443–457. doi:10.1016/0010–2180(94)90110–4.

[55] Mura, A. and Borghi, R., "Towards an extended scalar dissipation equation for turbulent premixed combustion," *Combust. Flame*, Vol. 133, 2003, pp. 193–196.

[56] Kuan, T. S., Lindstedt, R. P., and Vaos, E. M., "Higher moment based modeling of turbulence enhanced explosion kernels in confined fuel-air mixtures," *Advances in Confined Detonations and Pulse Detonation Engines*, edited by G. D. Roy, Torus Press, Moscow, 2003, pp. 17–40.

[57] Swaminathan, N. and Grout, R. W., "Interaction of turbulence and scalar fields in premixed flames," *Physics of Fluids*, Vol. 18, No. 4, 2006, pp. 045102.

[58] Chakraborty, N. and Swaminathan, N., "Influence of the Damköhler number on turbulence-scalar interaction in premixed flames. I. Physical insight," *Physics of Fluids*, Vol. 19, 2007, pp. 045103–1–10.

[59] Swaminathan, N. and Bray, K. N. C., "Effect of dilatiation on scalar dissipation in turbulent premixed flames," *Combust. Flame*, Vol. 143, 2005, pp. 549–565.

[60] Gomet, L., Robin, V., and Mura, A., "Influence of Residence and Scalar Mixing Time Scales in Non-Premixed Combustion in Supersonic Turbulent Flows," *Combustion Science and Technology*, Vol. 184, No. 10-11, 2012, pp. 1471–1501. doi:10.1080/00102202.2012.690259.

[61] Bressloff, N. W., "A parallel pressure implicit splitting of operators algorithm applied to flows at all speeds," *Int. J. Numer. Methods Fluids*, Vol. 36, 2011, pp. 497–518.

[62] Lee, S. B., "A study on temporal accuracy of OpenFOAM," *International Journal of Naval Architecture and Ocean Engineering*, Vol. 9, No. 4, 2017, pp. 429–438. doi:10.1016/j.ijnaoe.2016.11.007.

[63] Dutt, P., "Stable Boundary Conditions and Difference Schemes for Navier-Stokes Equations," *SIAM Journa of Numerical Analysis*, Vol. 25, No. 2, 1988, pp. 245–267. doi:10.1137/0725018.

[64] Poinsot, T. J. and Veynante, D., *Theoretical and Numerical Combustion*, Edwards, 2nd ed., 2005.

[65] Piomelli, U. and Balaras, E., "Wall-Layer Models for Large-Eddy Simulations," *Annual Reviews of Fluid Mechanics*, Vol. 34, No. 1, 2002, pp. 349–374. doi:10.1146/annurev.fluid.34.082901.144919.

[66] LeVeque, R. J., *Finite Volume Methods for Hyperbolic Problems*, Cambridge University Press, Cambridge, UK, 2007.

[67] Kee, R. J., Grcar, J. F., Smooke, M. D., Miller, J. A., and Meeks, E., "A Fortran Program for Modeling Steady Laminar One-Dimensional Premixed Flames," Tech. Rep. SAND85-8240, Sandia National Laboratories, Livermore, CA, 1985.

[68] Langella, I., Doan, N. A. K., Swaminathan, N., and Pope, S. B., "Subgrid scale velocity models for reacting and nonreacting flows," *Physical Review Fluids*, Accepted, 2018. doi:10.1103/PhysRevFluids.00.004600.

[69] Kemenov, K. A., Wang, H., and Pope, S. B., "Modelling effects of subgrid-scale mixture fraction variance in LES of a piloted diffusion flame," *Combustion Theory and Modelling*, Vol. 16, No. 4, 2012, pp. 611–638. doi:10.1080/13647830.2011.645881.

[70] Techer, A., Moule, Y., Lehnasch, G., and Mura, A., "Mixing of Fuel Jet in Supersonic Crossflow: Estimation of Subgrid-Scale Scalar Fluctuations," *AIAA Journal*, Vol. 56, No. 2, 2018, pp. 465–481. doi:10.2514/1.J056251.

Appendix A: Comparison with previous studies

The SGT-100 was also simulated using other combustion models in the past and it is worthwhile to cross compare the flamelet model, Case C in Table 1, statistics to the past results. Pertinent details of those studies are listed in Table A1 along with the corresponding symbols used for Figs. A1 to A6. The data published in earlier studies are obtained using professional digitising softwares having pixel-level resolution. The numerical grids used here and in [5] are the same but employed different finite volume based codes, OpenFOAM for the current study and BOFFIN in [5]. Further detail on the Eulerian stochastic fields method used in [5] can be found there. A partially stirred reactor model and OpenFOAM code were used in [6] with four different, 1-step, 4-step, 20-step and 25-step, chemical kinetics mechanisms and the results for 20-step and 25-step mechanisms showing the closest agreement to the measurements [19] are chosen for comparison here. Thickened flame model implemented in AVBP solver with a 22-step skeletal mechanism was used in [20].

The SGT-100 configuration was analysed by Fedina *et al.* [21] using OpenFOAM with about 7.5 M grid cells and six different combustion models: thickened flame (TF), stochastic fields, partially stirred reactor, eddy dissipation (ED), fractal and approximate deconvolution models. The results in [21] for the partially stirred reactor model are the same as those for model 3 in Table A1. Results for the stochastic field model in [21] are very similar to those shown here for model 2 of Table A1. Also, the statistics obtained in [21] using thickened flame, stochastic field, fractal and approximate decomposition models were found to be similar to each other. Because of this, the results for the four model used in [21] are not shown here. The TF model used in [21] is very similar to that used in [20] (model 5 in Table A1) with a substantially coarser mesh compared to that used in [21]. This and the ED model are also not shown here for clarity of the plots, but are commented in the discussion. Thus, the comparisons shown in Figs. A1 to A6 include the computational results available in the studies listed in Table A1. Although one may say that the statistics should not depend on the code and numerical schemes used it is quite well known that the LES results can have some sensitivity to these details and so one must be mindful of this while making cross comparisons.

The velocity statistics, mean and rms values, are compared in Figs. A1 and A2 for the axial and radial velocities respectively. The agreement among the numerical results and with measurements

Table A1: Summary of modelling detail

No.	Model	Mesh size	Mechanism	Reference	Symbol
1	Flamelet	8M	GRI 3.0	this study	—
2	Eulerian stochastic fields	8M	15-step	[5]	×
3	Partially stirred reactor	7M	20-step	[6]	– –
4	Partially stirred reactor	7M	25-step	[6]	□
5	Thickened flame	120M	22-step	[20]	– · –

are good for $\langle U \rangle$ at Loc. 1 and as one moves downstream, the difference among the numerical results do not change much but there is some over prediction compared to measurements in the inner shear layer region, ie., $20 \leq r \leq 40$ mm. However, a close study of Fig. A1 suggests that the results of Partially stirred reactor model with 20-step kinetics and thickened flame model with 22-step chemistry are closer to the measurements. The over prediction by other models suggests that there is some under estimate of the reactant jet expansion and its penetration inside the combustor leading to a narrower CRZ for the flamelet, Eulerian stochastic fields and partially stirred reactor model with 25-step chemistry. The results for TF in [21] show that there is a strong grid dependency for this model. The ED model in [21] was shown to yield improved results for mean axial velocity, which are comparable to those for the model 3 listed in Table A1 above. The predicted rms values agree quite well with measurements for Loc. 1 and for other locations all the models behave satisfactorily. Also, this is the case for the TF and ED models considered in [21] although the latter was observed to yield higher rms values. Overall, the axial velocity field is not strongly influenced by the combustion model, which was also noted in [21].

The radial velocity statistics computed using flamelet model agree quite well with those for the Eulerian stochastics field method and the measurements. Since the time-averaged flow is expected to be symmetric about the centreline the radial velocity should be $\langle V \rangle = 0$ at $r = 0$, which is captured well by the flamelet model. The experimental data show a negative velocity which is also observed for the Eulerian stochastic fields method used in [5]. The computed rms values compare quite well with measurements as seen in Fig. A2. Radial velocity obtained for the other combustion models

used in past studies of SGT-100 were not reported and thus they are not shown and discussed here.

Figure A3 shows the comparison of mixture fraction statistics. The Eulerian stochastic fields and thickened flame model captured the measured mean mixture fraction variations quite well while there is some over prediction of the peak value by the flamelet model. However, the former two models under predicted σ_ξ while the flamelet results agree quite well with measurements. As noted in section IV C, the fully mixed value of $\langle\widetilde{\xi}\rangle = 0.034$ for the incoming air and fuel flow rates is not captured within the measurement locations (see for Loc. 4) while the flamelet result suggests that values of $\langle\widetilde{\xi}\rangle > 0.031$ can occur for $r > 50$ mm to give the fully mixed value. This is not seen for the other two models. The sensitivity of the computed $\langle\widetilde{\xi}\rangle$ and σ_ξ to the incoming air and fuel flow rates within the measured uncertainties were assessed to be negligible for the current study. Hence, the over prediction is related to the under estimate of the jet expansion and penetration, and avenues to improve this will be explored in future studies. Overall, the velocities and mixture fraction statistics computed using the flamelet model are comparable to those observed in earlier studies. Note that the statistics obtained for other combustion models used in the past studies were not reported and thus they are not discussed here.

The temperature and reactive scalar mass fractions are compared in Figs. A4 to A6. The averaged temperature in the CRZ is over estimated by about 150 K in the past studies for Loc. 1 while the flamelet model value agrees well with measurements. However, the over prediction of the averaged temperature near $r \approx 40$ mm is similar to those observed in [5]. The level of this overestimate is reduced for the thickened flame model [20], however a significant overestimate was observed for the 7.5 M grid used in [21], which is similar to the results of the flamelet model. Thus, the improved comparison seen by Jaravel *et al.* [20] is because of their very fine grid (see Table A1) which may be able to capture the strain effects with no further modelling. The 20-step mechanism was shown to over predict the ignition delay times and under predict the extinction strain rates for the thermo-chemical conditions of the SGT-100 compared to the GRI 3.0 mechanism [6] and this could be a reason for the good match seen at $r \approx 40$ mm. This is supported by the temperature over prediction observed for the 25-step mechanism which yielded the ignition delay times and extinction strain rates comparable to those obtained using GRI 3 [6] and this temperature over prediction is

similar to the flamelet value as in Fig. A4. The ED model used in [21] showed a reduced overestimate for temperature at Loc. 1 and 2, which is comparable to that observed for the 20-step partially stirred reactor model (see Table A1. The difference among the computed averaged temperature reduces as one moves downstream, however there is a substantial difference for the temperature rms. Past studies show a considerably smaller rms values compared to measurements and flamelet values in general.

The peak averaged values of reactant species, CH4 and O2, are under predicted by the flamelet model compared to the measurements, which is consistent with the corresponding averaged mixture fraction value. The averaged CH4 values obtained for the flamelet and the PSR models are quite close to each other while the Eulerian stochastic fields method gave a lower value as seen in Fig. A5. Almost all the methane is consumed by Loc. 3 in the stochastic fields method while the measurements and the other two models show that there are some methane present at this axial location for $40 \leq r \leq 60$ mm. The other reactant species $\langle Y_{\mathrm{O2}} \rangle$ agrees quite well for the flamelet and Eulerian stochastic fields models as in Fig. A6 but there is some under estimate by both the models compared to measured values. The flamelet model values of $\langle Y_{\mathrm{H2O}} \rangle$ agrees well with measurements, except for the over prediction around $r = 40$ mm which is consistent with the temperature, mixture fraction and mass fractions of CH4 and O2. The Eulerian stochastic fields method seem to have over estimated the averaged water mass fractions. The relative variations of computed $\langle Y_{\mathrm{CO2}} \rangle$ are consistent with the other mass fraction values.

The species statistics are not reported for the thickened flame model of Jaravel *et al.* [20] and thus they are not shown here. This model used in [21] severely under predicted the reactant species (thus over prediction of products) for Loc. 2 to 4. However, the results of the ED model in [21] compared well with measurements. Overall, the flamelet model predictions are comparable to other methods but incurs lower computational cost.

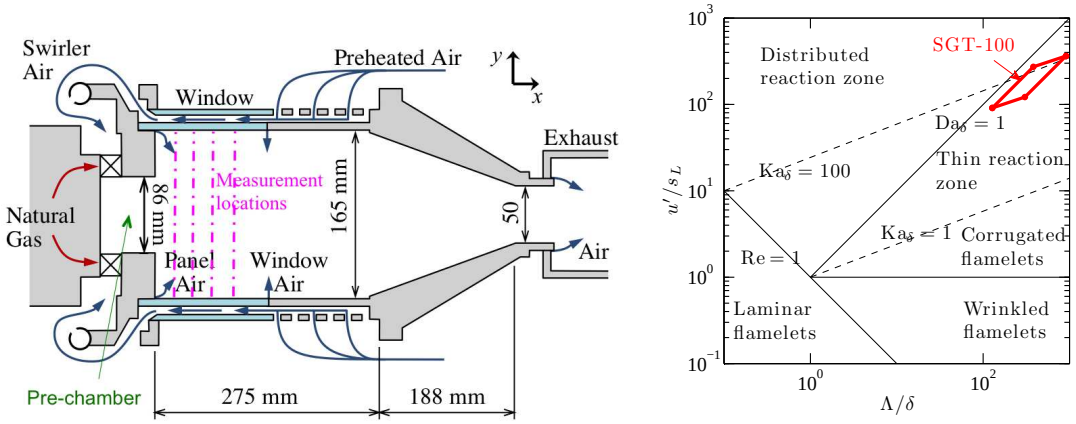

(a) (b)

Fig. 1: TurChemi (SGT-100) combustor (not to scale, after [19]) with stream wise positions for measurements (a). The combustion condition for the SGT-100 combustor is shown by the area indicated on the Borghi diagram in (b).

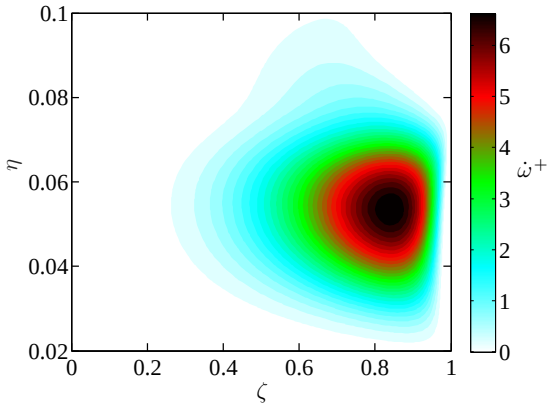

Fig. 2: Variation of normalised flamelet reaction rate, $\dot{\omega}^+$ with $\zeta = c$, and $\eta = \xi$. The reaction rate is normalised using unburnt gas density, δ_{th} and s_L for the flame with $\phi = 0.6$ ($\xi \approx 0.034$) mixture.

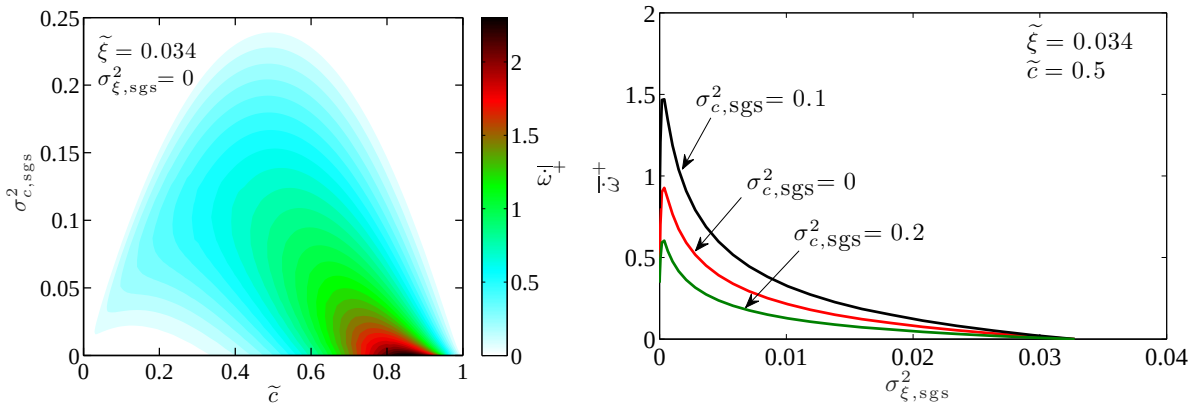

(a) (b)

Fig. 3: Variation of normalised filtered reaction rate, $\overline{\dot{\omega}}^+_{\mathrm{fp}}$, with $\widetilde{c}$ and $\sigma^2_{c,\mathrm{sgs}}$ for $\widetilde{\xi} = 0.034$ and $\sigma^2_{\xi,\mathrm{sgs}} = 0$ is shown in (a). The variation of $\overline{\dot{\omega}}^+_{\mathrm{fp}}$ with $\sigma^2_{\xi,\mathrm{sgs}}$ for $\widetilde{\xi} = 0.034$, $\widetilde{c} = 0.5$ and three different values of $\sigma^2_{c,\mathrm{sgs}}$ is shown in (b).

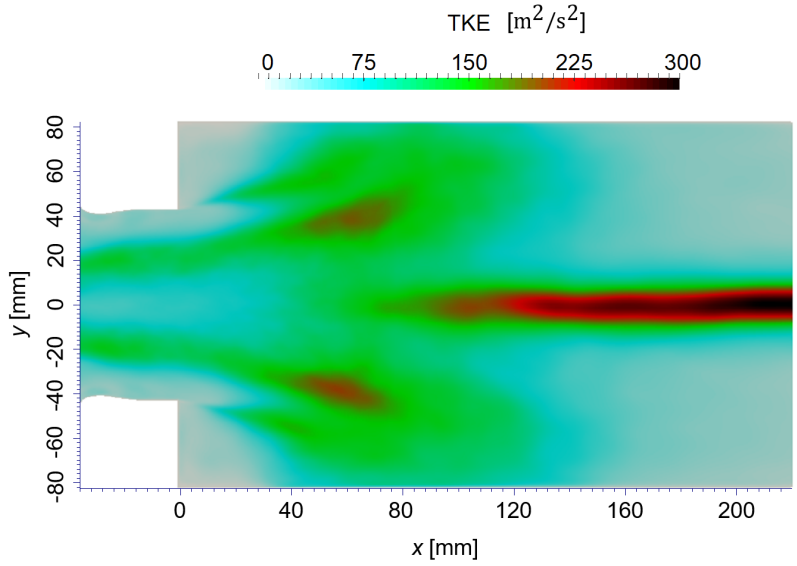

Fig. 4: Variation of time-averaged resolved turbulent kinetic energy per unit mass, $\langle \mathcal{K} \rangle$, in the mid-plane.

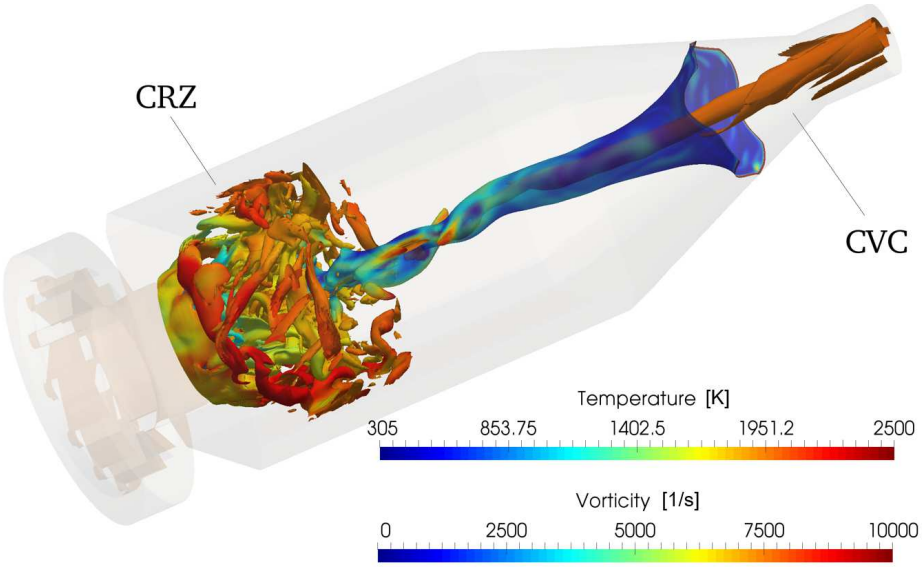

Fig. 5: Visualisation of computed flow structures using vorticity iso-surfaces (tubes) are coloured by temperature; pressure iso-surfaces (sheet) coloured by vorticity. The result is shown for Case C.

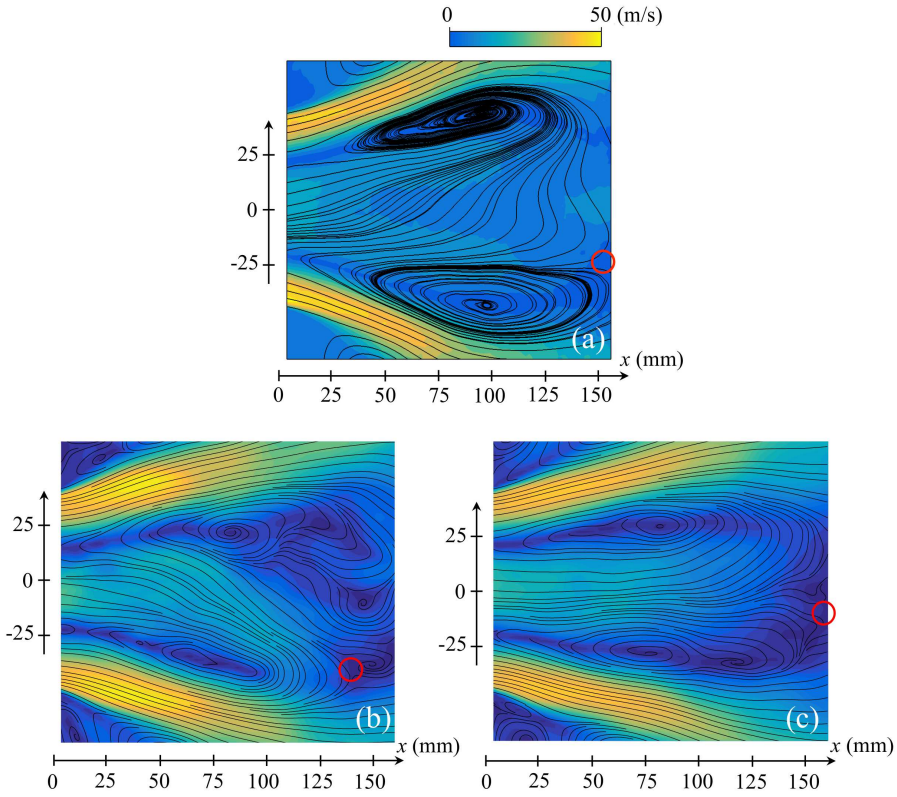

Fig. 6: Averaged magnitude of planar velocity (color map): (a) from PIV measurements [19] and LES results for (b) Case B and (c) Case C in Table 1. The corresponding streamlines are also shown. The computed rear stagnation point is marked with a circle.

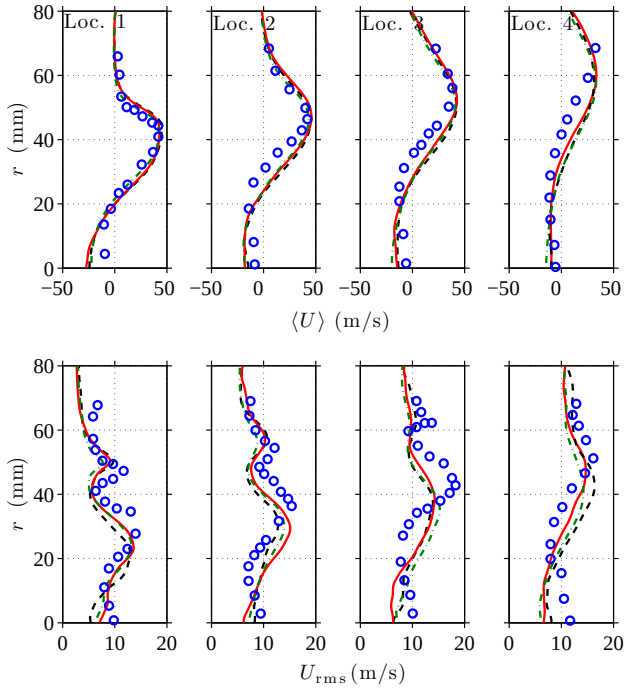

Fig. 7: Radial variations of mean and rms axial velocity: measurements (circles) and LES results for Cases A (– –), B (——) and C (– · –) in Table 1.

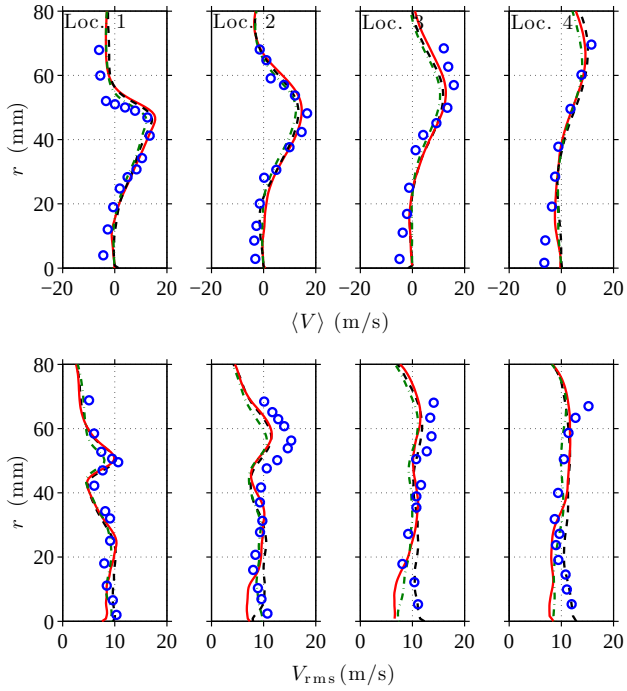

Fig. 8: Radial variations of mean and rms radial velocity: measurements (circles) and LES results for Cases A (– –), B (——) and C (– · –) in Table 1.

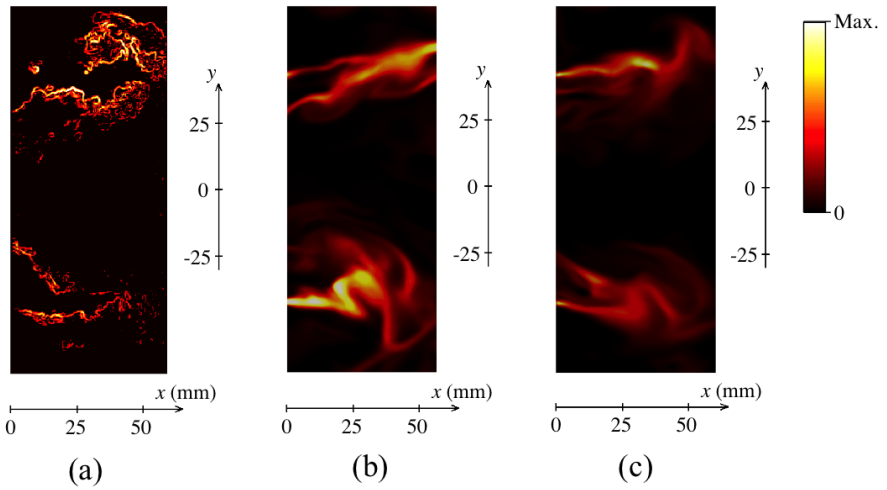

Fig. 9: A single snapshot OH-PLIF, coloured by OH gradient, in the mid-plane is shown in (a). Figures (b) and (c) show the mid-plane spatial variation of normalised reaction rate obtained in Case B and Case C respectively.

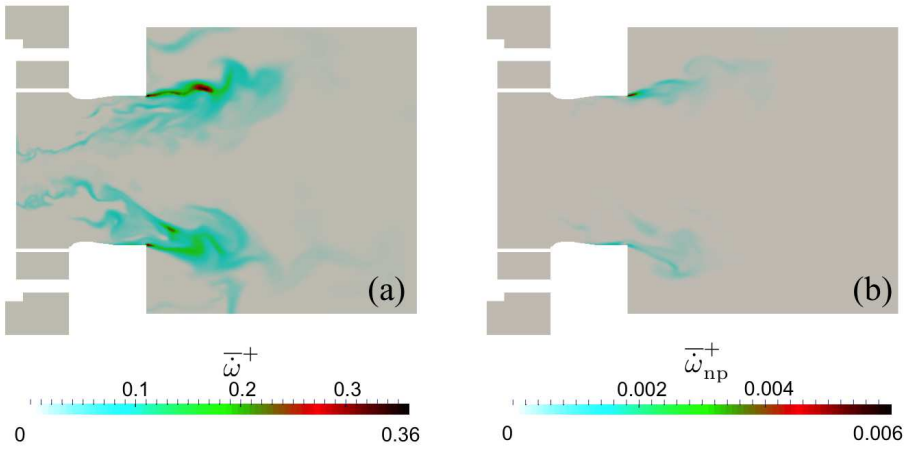

Fig. 10: Mid-plane spatial variations of (a) total normalised reaction rate and (b) non-premixed mode contribution, $\overline{\dot{\omega}}^{+}_{\mathrm{np}}$, for Case C.

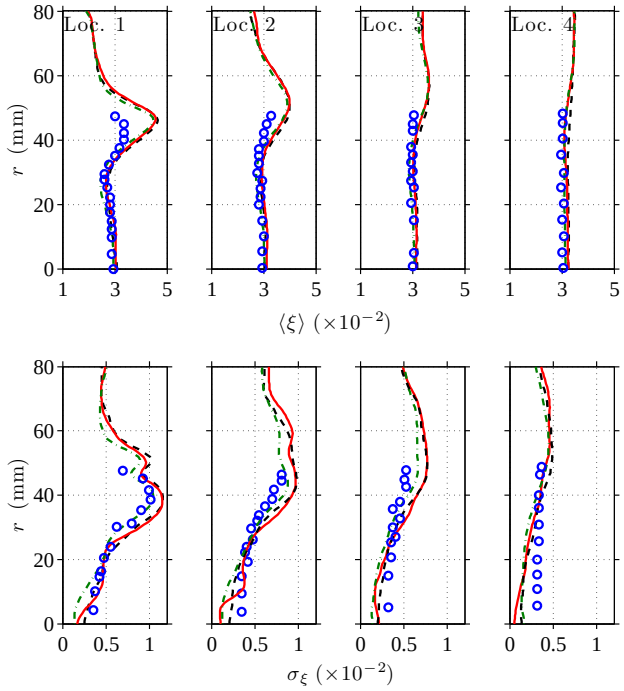

Fig. 11: Variations of mean, $\langle\xi\rangle$, and rms, σ_ξ, mixture fraction: measurements (circles) and LES results for Cases A (– –), B (——) and C (–·–·–).

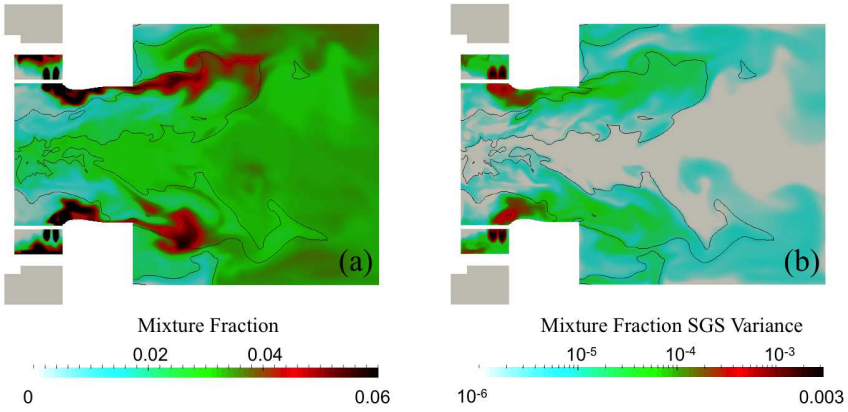

Fig. 12: Mid-plane contours of (a) mixture fraction and (b) its SGS variance for Case C. Two iso-lines of $\widetilde{c} = 0.05$ and 0.95 are used to mark the flame region.

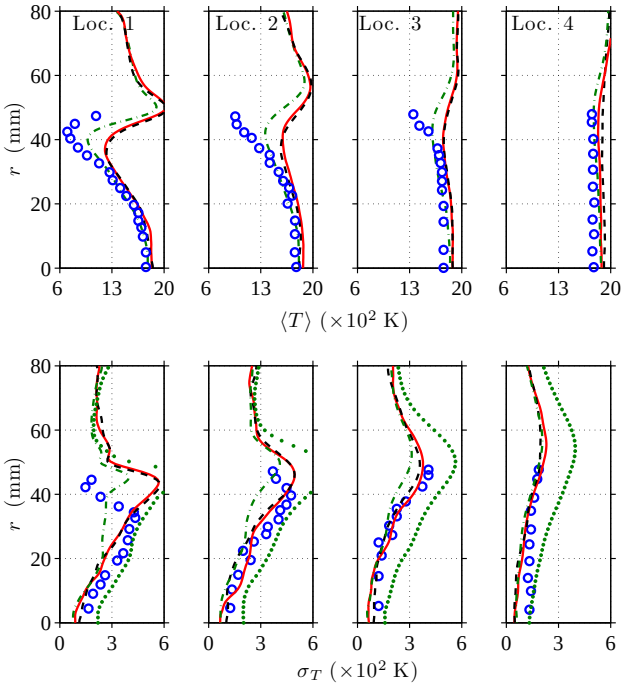

Fig. 13: Variations of mean and resolved rms temperature: measurements (circles) and current LES results for Cases A (– –), B (——) and C (–·–). Profiles of total rms temperature, $\sigma_{T,\mathrm{tot}} = \sqrt{\sigma^2_{T,\mathrm{res}} + \sigma^2_{T,\mathrm{sgs}}}$, where $\sigma^2_{T,\mathrm{res}}$ and $\sigma^2_{T,\mathrm{sgs}}$ are respectively the resolved and SGS temperature variances, is also shown (•••) for Case C.

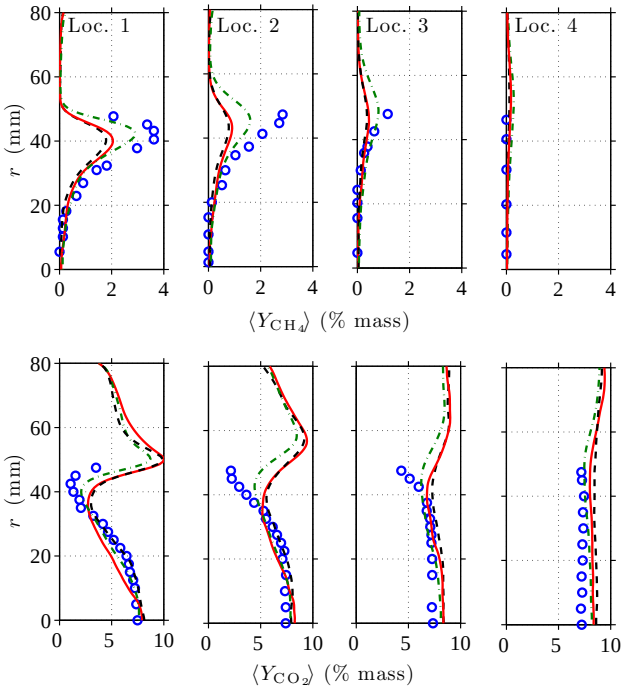

Fig. 14: Comparison of measured (circles) and computed, Cases A (– –), B (——) and C (–·–), mass fractions of CH_4 and CO_2.

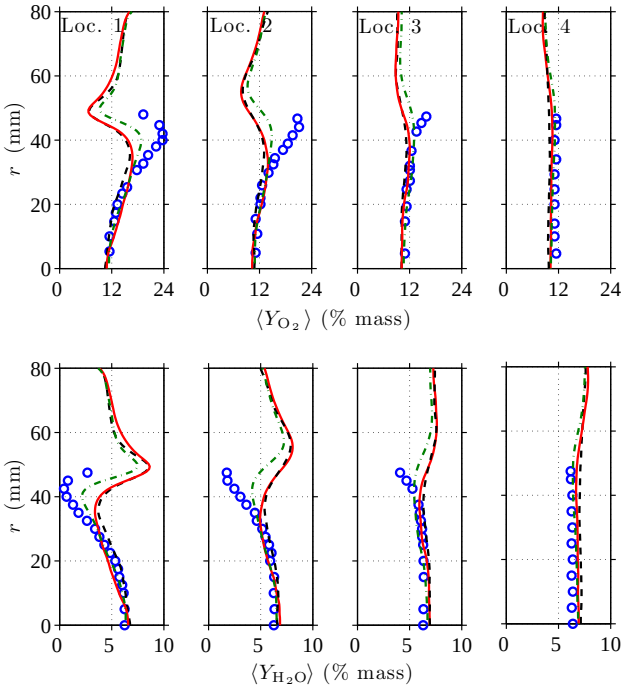

Fig. 15: Comparison of measured (circles) and computed, Cases A (– –), B (——) and C (–·–), mass fractions of O_2 and H_2O.

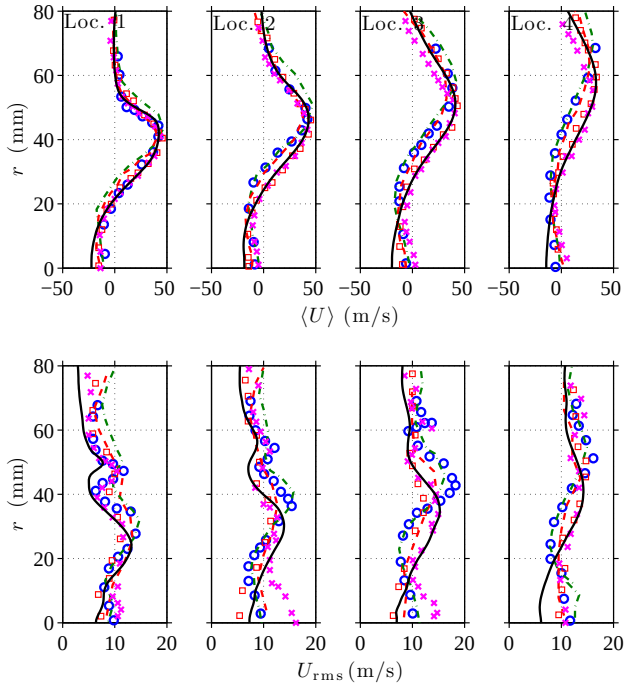

Fig. A1: Comparison of mean and rms of axial velocity: measurements (circles) and the legends for the computational results are shown in Table A1.

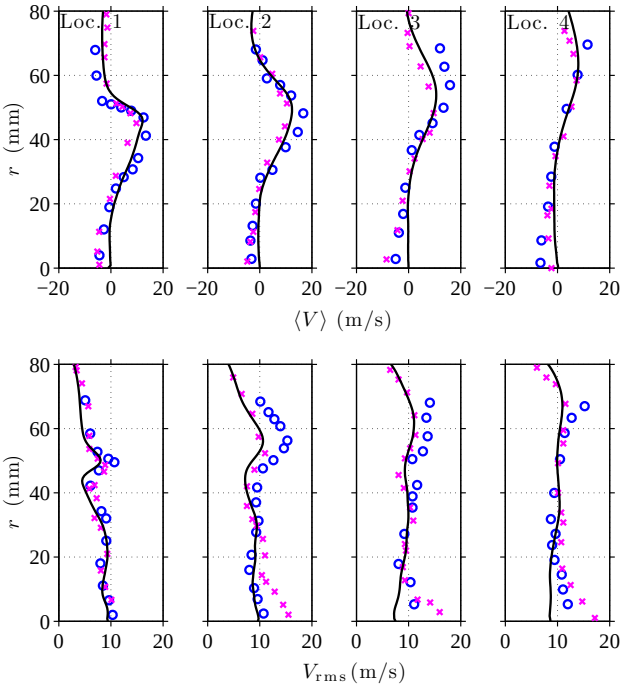

Fig. A2: Comparison of mean and rms of radial velocity: measurements (circles) and the legends for the computational results are shown in Table A1.

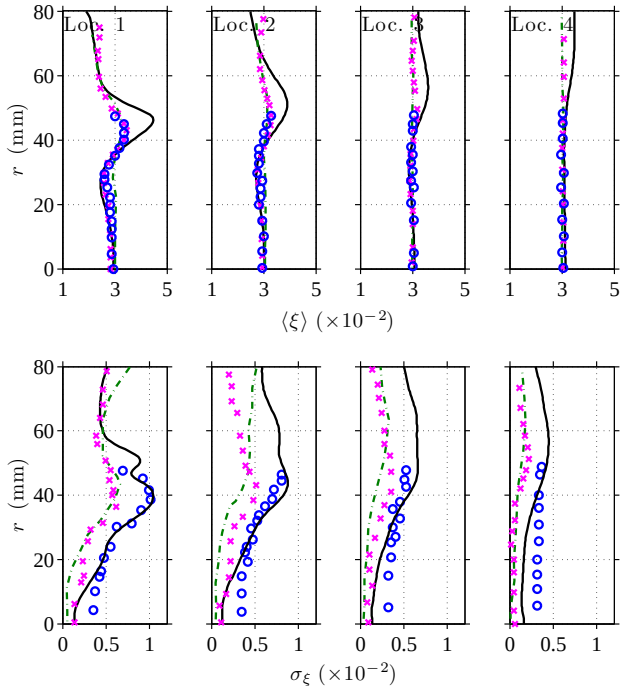

Fig. A3: Comparison of mean, $\langle\xi\rangle$, and rms, σ_ξ, mixture fraction: measurements (circles) and the legends for the computational results are shown in Table A1.

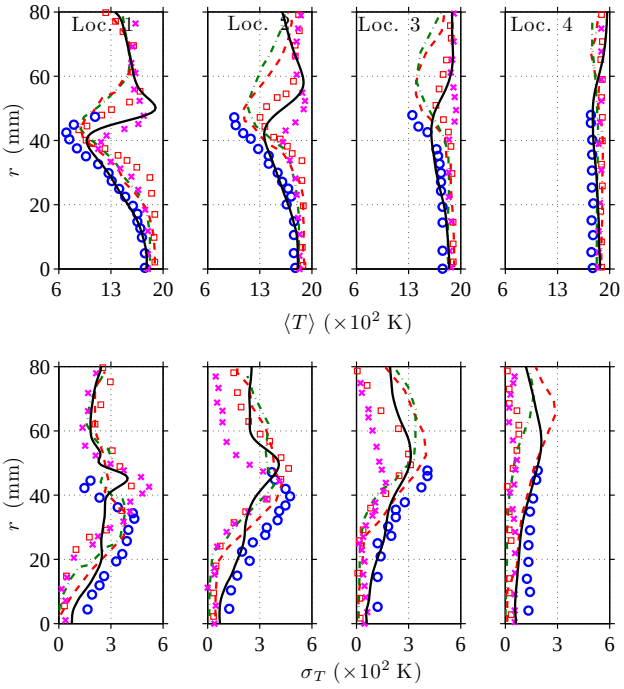

Fig. A4: Variations of mean and rms temperature: measurements (circles) and the legends for the computational results are shown in Table A1.

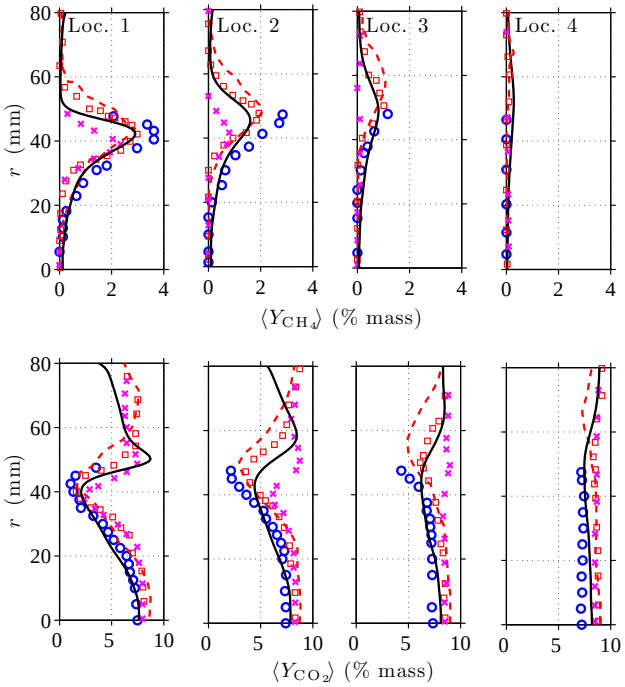

Fig. A5: Radial variations of CH_4 and CO_2 mass fractions: measurements (circles), and the legends for the computational results are shown in Table A1.

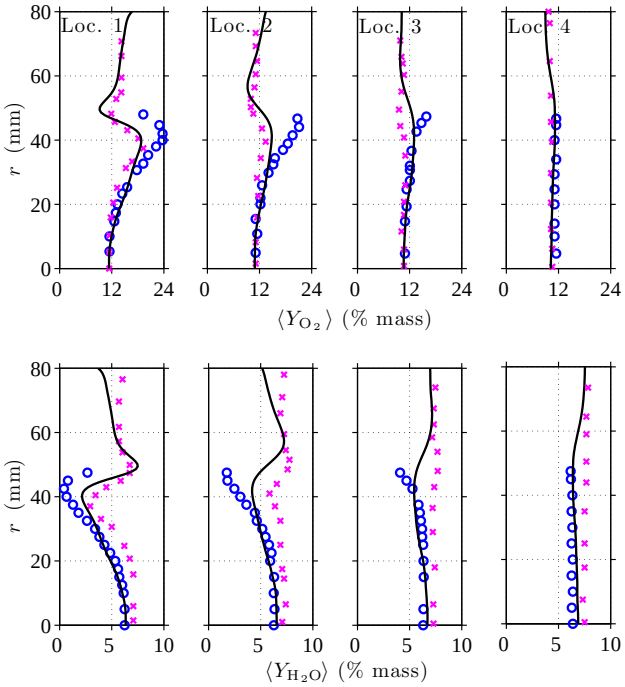

Fig. A6: Comparisons of O_2 and H_2O mass fractions: measurements (circles), and the legends for the computational results are shown in Table A1.